Traversing Sea Ice—Linking Surface Roughness and Ice Trafficability Through SAR Polarimetry and Interferometry

Dyre Oliver Dammann, Hajo Eicken, Andrew R. Mahoney, Eyal Saiet, Franz J. Meyer, *Member, IEEE*, and John C. "Craig" George

***Abstract*—Arctic landfast sea ice is widely utilized for transportation by local communities and industry, with trafficability largely governed by ice roughness. Here, we introduce an approach to evaluate ice roughness that can aid in routing of ice roads and assessment of spatial variability and long-term changes in trafficability. Drawing on synthetic aperture radar (SAR) polarimetry, SAR interferometry (InSAR), and other remote sensing techniques, we integrated approaches into the trafficability assessment that had rarely been applied over sea ice in the past. Analysis of aerial photogrammetry obtained through structure-from-motion helped verify cm-scale accuracy of X-band InSAR-derived ridge height and link L-band polarimetric classification to specific roughness regimes. Jointly, these approaches enable a km-scale evaluation of ridge topography and cm- to m-scale roughness—both critical for the assessment of trafficability. A trafficability index was derived from such SAR data in conjunction with analysis of ice trail routing and ice use near Utqiaġvik, Alaska. The index identifies areas of reduced trafficability, associated with pressure ridges or rubble ice, and served to delineate favorable trail routes for different modes of transportation, with potential uses ranging from ice road routing to emergency evacuation. Community outreach is needed to explore how this approach could assist different ice users in reducing risk, minimizing trail or ice construction efforts, and improving safety.**

***Index Terms*—Radar interferometry, radar polarimetry, sea ice, surface roughness, surface topography, synthetic aperture radar.**

I. Introduction

A. Sea Ice Roughness and Implications for Sea Ice Travel and On-Ice Operations

LANDFAST sea ice provides a range of services to people, marine mammals, and the broader ecosystem around the circumpolar North [1]. This relatively narrow belt of ice is attached to the coast and serves as an extension of the land used for community travel and subsistence activities [2]–[6]. Landfast ice also serves as a platform for ice road construction by the industry [7]–[10]. Over the past few decades, landfast sea ice has undergone rapid decline in extent and seasonal persistence [11], [12] associated with Arctic-wide sea ice retreat [13]–[15]. At the same time, coastal community dependence on ice-based transportation has increased due to higher alternate transportation costs, greater removal of subsistence resources, and a growing industrial presence (9.4.5 in AMAP [16]). The potential socio-economic implications of these developments [17] require research progress to aid in adaption or mitigation of change [18].

Mapping of local ice use [3], [19]–[22] and studies of environmental change impacts on coastal communities have progressed significantly [5], [23]–[27]. Such progress includes new methods to monitor ice conditions relevant to ice use and to provide guidance to ice users [3], [28], [29]. However, so far, quantitative approaches to analysis and hazard assessment of ice conditions relevant to IR and trail use, and applicable over larger scales and across seasons have been lacking.

This work focuses on ice roughness at scales of 0.1–10 m, which is a key factor determining the use of landfast ice for transportation by local residents [2], [22], [24], industry [30], and in the context of potential emergency evacuation from industrial installations and winter vessel traffic [31]–[33]. Ice roughness is relevant in routing and construction of ice trails and roads due to the negative impacts of rough ice on travel time and cost through increased road length by avoiding rough areas, surface preparation cost, equipment wear, etc. However, grounded pressure ridges, typically the largest roughness elements in the landfast ice cover, help stabilize the ice, thereby potentially reducing the hazards of ice travel [34]–[36].

Landfast ice can form through *in situ* freezing in the coastal zone, the advection of ice formed offshore, or a combination of these two processes. Landfast ice formed through *in situ* freezing typically will be smooth, though wind and ocean stress or interaction with drifting pack ice may increase its roughness. Landfast ice advected from offshore may be deformed already, or deform during the attachment process. In addition to amplitude, ranging up to the m-scale, roughness can be identified by the wavelength of the roughness features. We define short-wave

Manuscript received April 10, 2017; revised September 8, 2017; accepted October 8, 2017. Date of publication December 24, 2017; date of current version February 12, 2018. This work was supported in part by the National Science Foundation (Seasonal Ice Zone Observing Network, NSF-0856867), in part by the Alaska Center for UAS Integration, and in part by the Swedish National Space Board (Dnr 192/15). *(Corresponding author: Dyre O. Dammann.)*

D. O. Dammann was with the Geophysical Institute, University of Alaska Fairbanks, Fairbanks, AK 99775 USA, and is now with the Department of Space, Earth, and Environment, Chalmers University of Technology, Gothenburg 412 96, Sweden (e-mail: dyre.dammann@chalmers.se).

H. Eicken is with the International Arctic Research Center, University of Alaska Fairbanks, Fairbanks, AK 99775 USA (e-mail: heicken@alaska.edu).

A. R. Mahoney, E. Saiet, and F. J. Meyer are with the Geophysical Institute, University of Alaska Fairbanks, Fairbanks, AK 99775 USA (e-mail: armahoney@alaska.edu; ejsaiet@alaska.edu; fjmeyer@alaska.edu).

J. C. George is with the North Slope Borough Department of Wildlife Management, Utqiaġvik, AK 99723 USA (e-mail: craig.george@north-slope.org).

Color versions of one or more of the figures in this paper are available online at http://ieeexplore.ieee.org.

Digital Object Identifier 10.1109/JSTARS.2017.2764961

1939-1404 © 2017 IEEE. Personal use is permitted, but republication/redistribution requires IEEE permission.
See http://www.ieee.org/publications_standards/publications/rights/index.html for more information.

TABLE I
THERMAL AND DYNAMIC PROCESSES AND RESULTING ROUGHNESS TYPES AND SCALES

	Process	Roughness
Thermal	Ice freezing in-place during calm conditions	Smooth ice or cm-scale LW roughness
	Ice freezing in-place during rough ocean conditions resulting in consolidation of slush or pancake ice	cm-scale SW roughness
	End-of-season surface melt processes and melt pond formation	cm-scale LW roughness
	Multiyear ice forming in place	cm or m-scale LW roughness with potential large vertical relief between regions of multiyear and first-year ice
Dynamic	Displacement of thinner ice («1 m) resulting in fractures, moderate buckling, and rafting	cm-scale LW roughness in the form of sporadic features of cm-scale vertical extent
	Thicker ice (∼1 m) yielding under severe forcing conditions resulting in rearranging orientation of floes into the vertical	m-scale continuous or noncontinuous areas of SW roughness in the form of rubble fields or ridges
	Advection of first year or multiyear pack ice into the region and freezing into landfast ice	Roughness depends on conditions under initial formation and transport

roughness (SW), where the ratio of amplitude to wavelength is close to one, and long-wave roughness (LW), where amplitude is much smaller than the wavelength.

Small-scale roughness of sea ice can be determined by the sea state during the early stages of freeze-up. Initial freezing during calm conditions will result in smooth nilas, while a choppy sea will result in cm-scale SW roughness (e.g., pancake ice). Potentially small-scale roughness inherent in the ice since freeze-up will remain as the ice grows thicker. While the ice is still thin, it is subject to cm-scale roughness features due to rafting and buckling. Rafting will result in roughness in the form of a step in the leading edges of the rafting floes [37], while buckling will often impart LW roughness features to ice smooth on shorter length scales. As the ice approaches meter-scale thickness, it is strong enough to resist moderate forces, but is still subject to deformation under substantial forcing events such as pack ice.

Interaction with pack ice can result in grinding of ice in the shear zone between pack ice and the landfast ice edge or coastline [28], resulting in rough ice. Forces can also propagate further into the landfast ice, leading to aggregation of ice fragments into rubble and potentially ridges. Here, the ice bottom in combination with the sea floor can channel currents beneath the ice, which may play an important role weakening ice and predisposing it to deformation [35], [38]. During spring and summer, melt pond formation will result in cm-scale LW roughness features, which if surviving multiple summers will turn into multiyear ice with potential m-scale roughness with a longer wavelength as melt ponds deepen leading to increased relief of adjacent bare ice [39]. The different surface roughening processes and the associated scales and types of roughness are listed in Table I.

It is reasonable to assume that sea ice roughness has increased throughout the Arctic in recent years as a result of

1) increased deformation due to thinner ice [40] and higher ice drift speeds [41], [42],
2) increasing ice strain and fracture [43],
3) increasing storm activity [44], and
4) later formation of landfast sea ice [12] when storms are the strongest [44].

The effects of increased roughness on ice travel, including associated hazards [25], are already felt in some regions [22], [24]. A particular concern is inconsistent freezing progression; instead of forming once, the ice continues to melt, break apart, and drift out during fall leading to rougher ice [22].

To date, quantitative assessments or projections of Arctic sea-ice trafficability are mostly lacking. Stephenson *et al*. [45] used modeling to understand how accessibility may change for shipping and ice roads on land. Due to increasing dependence on sea ice travel in combination with landfast sea ice change, it has become important to be able to evaluate changes in trafficability across sea ice, and in particular, sea ice roughness on scales critical to ice users. Here, we focus strictly on traveling over ice and hence define trafficability as the ability to travel on the sea ice surface in terms of efficiency and required effort. Factors impacting safety such as ice thickness or fractures are not considered here; trafficability is strictly dependent on surface conditions, in particular, roughness. This paper aims to classify and quantify ice roughness, yielding data products in support of tactical and long-term strategic decisions for on-ice operations and travel.

B. Remote Sensing Strategies to Assess Sea Ice Roughness

Ice users in coastal communities typically assess ice roughness visually at ground level. Maps delineating areas of rough ice based on radar satellite imagery have proven useful as qualitative supplemental information in several communities [28], [34], [46]. Oil and gas industry also commonly evaluate roughness strictly qualitatively through aerial reconnaissance [7]. However, tactical decisions on timescales from days to weeks (e.g., ice road routing, evacuation route planning) require quantitative roughness assessments [32] obtained in a cost-effective and timely manner [10]. To date, ice roughness and trafficability assessments predominately comprise *in situ* observations with limited spatial and temporal coverage [7], [28], [30]. Recent advances in satellite remote sensing set the stage for more comprehensive, efficient trafficability assessments compared to aerial reconnaissance (including human image interpretation [47] or ground truth [28]).

Seasonal planning and tactics of on-ice operations require repeat surveys with m- to dm-scale resolution at intervals of days to weeks covering the entire area of interest. Ice roughness information can be obtained through several methods, includ-

ing LIDAR, stereo-photogrammetry, and synthetic aperture radar (SAR). However, only SAR meets all the requirements of operational planning and tactics. The narrow swath width and long repeat intervals of space-borne Lidar instruments [48] and the poor spatial overlap of high-resolution imagery from, e.g., WorldView/Digital Globe [49] and their dependence on clear-sky conditions render both these approaches unsuitable for operational and many ice roughness research applications.

SAR signals are sensitive to surface roughness: Rough surfaces contain more scattering elements than smooth ice, resulting in a larger radar backscatter cross-section. With resolution on the order of 1–10 m, wide coverage from multiple platforms, independence of weather conditions, and repeat cycles of days to weeks, SAR is well-suited for operational use. Over some sea ice types, some of the microwave energy penetrates below the surface and is subject to volume backscatter from internal structural elements that does not necessarily indicate roughness. Here, SAR polarimetry (see Section II-E) and interferometry (see Section II-F) may help in further discriminating between different backscatter mechanisms and type and size of roughness features. We validate these two techniques over sea ice, employing ground truth observations to evaluate the accuracy of the polarimetric classification [50], [51] and the interferometric digital elevation model (DEM) (see Sections III-A and III-B).

For the purpose of validation, we acquired images with an unmanned aerial system (UAS) to construct a high-resolution image mosaic and a DEM using structure-from-motion photogrammetry (SfM) (see Section II-C). SfM has shown promise in geoscience applications [52]–[54], including cm-resolution reconstruction of snow surface features [55]. This study focuses on the landfast sea ice near Utqiaġvik, Alaska (formerly known as Barrow, Fig. 1) as a test region. Landfast ice at Utqiaġvik typically spans a range of roughness types, from large grounded ridges to smooth ice. Utqiaġvik is the site of extensive ice use, with construction of a network of seasonal ice trails that occupy areas of higher trafficability [3]. Drawing upon GPS surveys of these trails, combinations of SAR techniques are used to develop a large-scale ice roughness and trafficability assessment strategy (see Sections III-C–III-E).

II. Data and Methods

The study focus is on landfast ice near Utqiaġvik, Alaska, and both *in situ* and space-borne data acquisitions occurred in March to May 2015 (see Fig. 1). Satellite products from three different SAR systems were utilized: TerraSAR-X and TanDEM-X operated by the German Aerospace Center (DLR) since 2008 and 2010, respectively, with a repeat pass cycle of 11 days, and Japanese Advanced Land Observing Satellite (ALOS-2) PALSAR-2 operating since 2014, with a repeat pass cycle of 14 days. UAS SfM data were acquired in collaboration with the Alaska Center for UAS Integration (ACUASI). Remote sensing datasets acquired are listed in Table II and discussed further below.

Most of the data were collected within roughly a week, but with the TerraSAR data obtained almost four weeks prior to acquisition of the SfM dataset. Based on the previous landfast ice reconnaissance in January 2015, we were able to confirm that the landfast ice surveyed had remained stationary during spring and hence did not noticeably change roughness between acquisitions. All data were acquired prior to the onset of melt; hence, potential cm-scale change in roughness as a result of snow accumulation and redistribution would only have a minor impact on the SAR signals and our analysis.

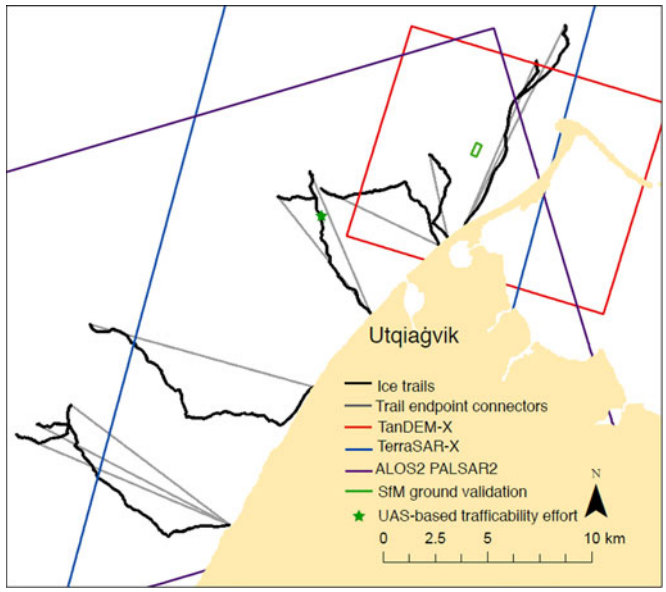

Fig. 1. Map of ice trails (black) close to Utqiaġvik, Alaska, during spring 2015 as well as trail endpoint connectors (gray). The colored rectangles show the coverage of SfM (green), TanDEM-X (red), TerraSAR-X (blue), and PALSAR (purple).

A. *In Situ Data*

Every spring, members of the community of Utqiaġvik construct trails leveling several mile-long corridors through the rugged landscape of the landfast ice using only hand tools [34]. These trails are essential to the community, providing subsistence hunters access to marine mammals and birds. Trail construction and use are also an important part of Iñupiaq traditional instruction and subsistence culture [1]. University of Alaska Fairbanks sea ice researchers have collaborated with Iñupiaq sea-ice experts and hunters and local organizations, including the Barrow Whaling Captains Association and the North Slope Borough Department of Wildlife Management, in mapping these community ice trails starting in spring 2000 and consistently every spring starting in 2007. Iñupiaq ice observers and hunters have also shared indigenous and local knowledge in regards to ice properties that are directly relevant or even critical for the construction and safety of operations on the ice trails during spring [3], [56]–[59].

The trail data used here include trail location and continuous ice thickness measurements along the trails. The latter were collected with an EM-31 electromagnetic conductivity meter linked with a GPS pulled by a snowmobile, described in detail by Druckenmiller [60]. The trail data were collected in April

TABLE II
LIST OF REMOTE SENSING DATASETS ANALYZED

Product	Platform	Sensor	Date	GSI (m)	Dir./mode	Additional info
Structure-from-motion	Ptarmigan UAS	DSLR	04/10/2015	0.11	–	Optical
Polarimetry	ALOS-2 PALSAR-2	SAR	04/02/2015	10	Ascend/Stripmap	Polarizations HH, HV, VH, VV
Interferometry	TanDEM-X	SAR	04/10/2015	2.35	Descend/Stripmap	Baseline 477 m
Backscatter	TerraSAR-X	SAR	03/14/2015	2.75	Descend/Stripmap	

GSI refers to the ground sampling interval.

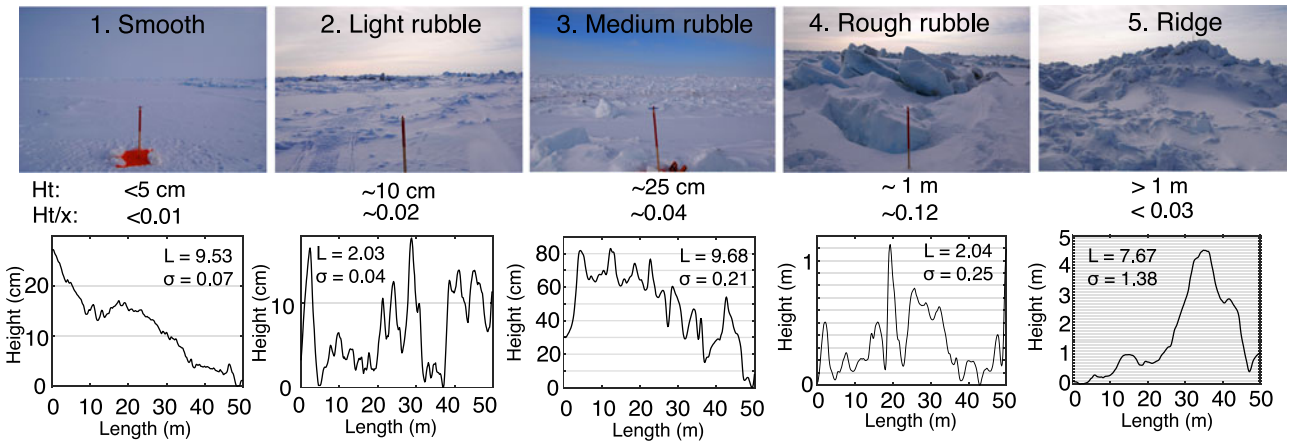

Fig. 2. Images of the five roughness categories encountered during ground validation with 50 m long height transects from the individual locations obtained from SfM DEM. Autocorrelation length (L) and standard deviation (σ) are listed for each transect and approximate values for roughness amplitudes and the ratio of feature height (Ht) vs. feature spacing (x) are listed for each roughness class.

and May of 2015, extending out along the coast within approximately 15 km from Utqiaġvik (black lines shown in Fig. 1). The trail crews draw on indigenous knowledge to construct the trails [3]. The trail path is carefully selected and often routed through stretches of level ice reducing the trail making effort in terms of time and financial costs. However, trails also favor areas of grounded ridges, which help anchor the landfast ice, in order to reduce the risk of break-out events (i.e., detachment of large pieces of ice from the landfast ice). More details of ice properties impacting trail locations can be found in the study by Druckenmiller *et al*. [3].

For our analysis, we investigated all ten trails constructed for the 2015 spring season. Trail location and ice thickness were sampled by GPS and EM every second along the trails; hence, point spacing is dependent on the speed of the snowmobile (roughly every 5 m). The trail is oversampled to construct equal sampling intervals (1 m) for every trail. Ten endpoint connectors (gray lines in Fig. 1) are constructed in a straight line from start to end of each trail (1 m sampling interval). These connectors are constructed as an estimate of hypothetical trail location independent of ice conditions impacting trail construction.

Additional *in situ* measurements include laser surveying of transects [30] as well as operation of a survey grade GPS system (Trimble 5700) to assess the quality of the SfM data. A total of 15 ground control points were also included to aid identification of important features such as ridge summit, transect boundaries, and roughness features with significance for trafficability. Two transects were profiled at equidistant intervals to evaluate the SfM performance, one across the ridge summit (5 m spacing) and one over barely navigable rubble-ice (20 cm spacing).

B. Classifying Sea Ice Roughness From a Trafficability Perspective

In Section I, we identified thermal and dynamic processes that govern surface roughness regimes on landfast ice. Here, we focus on those roughness types found at our study site, which are all associated with dynamic deformation of first-year sea ice. The roughness regime is similar to that described by Barker *et al*. [32] and hence we are applying a similar categorization of smooth, rubble (light, medium, and rough), and ridges, encompassing the roughness types found in our SfM data (see Fig. 2). Rubble is defined as an area of extremely deformed sea ice of unusual thickness formed during the winter by the motion of drift ice against, or around a protruding rock, islet, or other obstruction [61]. Here, we define smooth ice as exhibiting roughness features (H_t) 5 cm high or less (#1 in Fig. 2). Light rubble has a roughness of vertical relief of up to roughly 10 cm and can consist of scattered fragments of thinner ice (#2). We define medium rubble as scattered larger block sizes with a vertical relief on the order of tens of cm (#3). We identify rough rubble (#4) as continuous rubble with large vertical relief approaching maximum ice thickness (H_i). Ridges are roughness features exceeding ice thickness consisting of stacks of ice blocks. Roughness categories and their impact on trafficability are listed in Table III.

TABLE III
TYPES OF ICE ROUGHNESS AND IMPACT ON TRAFFICABILITY

Class (see Fig. 2 for details)	Impact on trafficability	Typical scale of roughness features
Smooth ice	Favorable for all transportation	$<$5 cm
Light rubble	Unproblematic for snowmobiles with thin snow layer, but impacts speed of cars on cleared ice roads	$<$10 cm
Medium rubble	Slows down transportation or requiring circumnavigation of features in ATV use and can be a direct obstacle for cars	Tens of cm
Rough rubble	Resulting in obstructed travel with ice modification necessary for all modes of transportation	$\sim$1 m
Ridges	Large ridges can result in obstructed travel and significant ice modification is needed	$>$1 m

The roughness of multiyear sea ice is different from that of first-year sea ice, typically comprising roughness elements of longer wavelength roughness, with high freeboard further limiting trafficability. However, due to the regional decline in multiyear ice and its absence in the 2015 landfast ice, it is not included as a separate category in this study.

Snow plays an important role in terms of the surface roughness of the ice and hence for trafficability at least in winter and early spring before snow-melt. Snowfall on smooth ice will, under calm wind conditions, result in a smooth snow surface substantially improving conditions for snowmobile travel. However, under strong winds, roughness can increase through wind redistribution of accumulated snow ranging from cm-scale ripple marks to dm-scale sastrugi. Through sintering, snow dunes can harden and become permanent roughness features [28], [62] inhibiting surface travel. On the other hand, over rough ice, snow generally reduces roughness by filling cavities between larger roughness features, hence increasing trafficability.

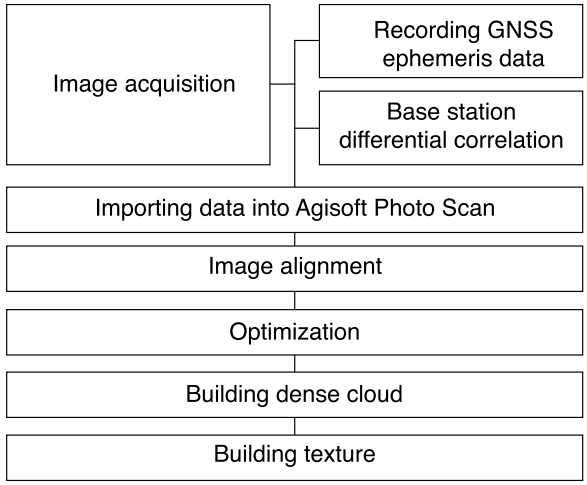

Fig. 3. Structure-from-motion processing workflow.

C. Structure-From-Motion Acquisitions

A UAS-based SfM dataset was acquired to be able to evaluate the ice roughness relevant to trafficability. High-resolution aerial imagery was acquired using a hexacopter UAS carrying a downward looking digital mirror-less camera (Sony NEX-7) and a Novatel survey grade Global Navigation Satellite System (GNSS). Using this system, we surveyed an area of roughly 200 m $\times$ 600 m (green rectangle centered in the red rectangle in Fig. 1) from an altitude of roughly 100 m. This altitude allowed for a high spatial resolution of roughly 10 cm required for a detailed trafficability analysis (see Section II-D).

The Novatel GNSS recorded the ephemeris data from both GPS and GLONASS satellites. An Arduino processor was used to orchestrate simultaneous acquisitions of data from both the camera and GPS at a 1 s interval. Photo acquisition intervals resulted in overlap between data take of roughly 90% (along-track) and 60% (cross-track). The acquisitions were obtained during the middle of the day to ensure optimum lighting conditions. The data were collected within a period of roughly 3 h to minimize changes in lighting conditions and ground shadows.

Data acquisition and processing workflows are outlined in Fig. 3. Two data products were generated: 1) a high-resolution orthorectified image mosaic [see Fig. 4(a)] and 2) a DEM [referred to from here on as SDEM, Fig. 4(b)] each with 11 cm ground sampling interval. The GNSS Ephemeris data were postprocessed (differential correction) using Novatel GrafNAV software (with Barrow airport as the base station) to achieve a DEM with high localization accuracy. The SfM processing was performed using Agisoft Photo Scan software.

D. Quantifying Sea Ice Roughness From UAS

When considering trafficability, the height (H_t) of features (i.e., amplitude) is critical and can be evaluated using the standard deviation σ, which describes the terrain's deviation from a level surface:

$$\sigma = \sum_{i=1}^{N}\sum_{j=1}^{N}\sqrt{\frac{\left(h_{i,j}-\bar{h}\right)^2}{N^2}} \tag{1}$$

where $h_{i,j}$ is the height in a particular pixel within a patch of $N \times N$ pixels with a mean height ($\bar{h}$).

Since standard deviation does not determine the roughness length-scale such that different structures can yield the same σ, the autocorrelation length (L) can be computed to evaluate the spatial variability [63]–[65]. We utilize Moran's *I* [66], as a

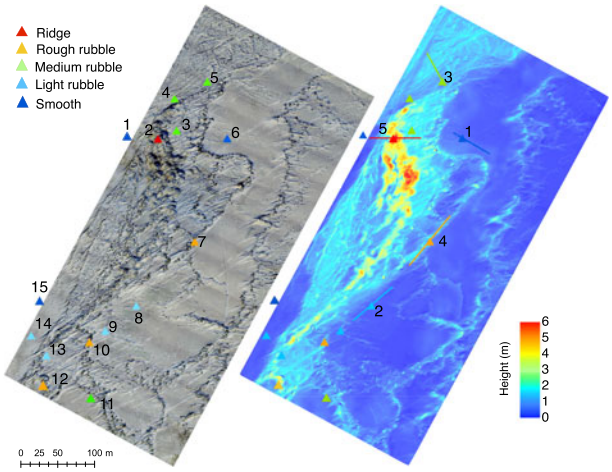

Fig. 4. (a) UAS-acquired image mosaic illustrates several different roughness regimes from a large ridge to level smooth ice. Triangles show locations of ground control points indicating type of roughness on the ground (warm colors represent rougher and cool represent smoother ice). Subtle shadow lines extend across the width of the image, which is an unresolved artifact from the SfM processing. (b) SDEM with lines indicating the location of transects shown in Fig. 2.

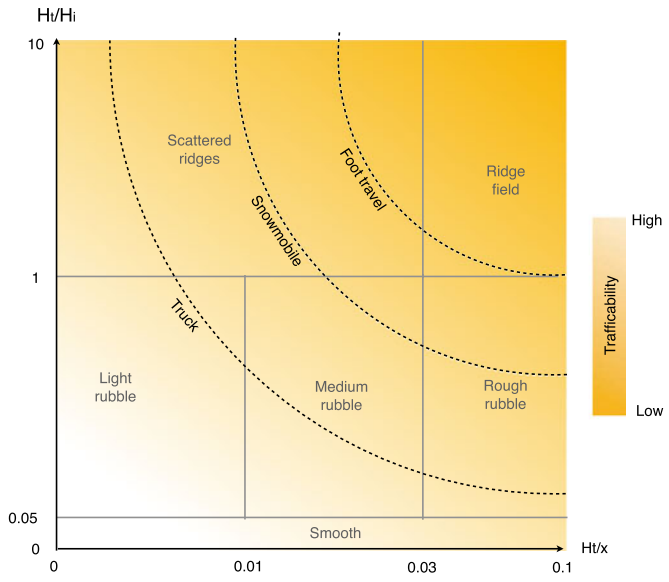

Fig. 5. Feature height and spacing shown as a parameter plane with different roughness categories occupying different sections of the plot (boundaries shown as schematic approximations). H_t is the topographic relief of ice features, H_i is the ice thickness (proxy for block size), and x is the wavelength (distance between features). Level of trafficability is roughly indicated in color shading as well as the approximate area, which can be traversed using different modes of transportation.

commonly used measure of spatial autocorrelation [67], [68]

$$I = \frac{N^2}{\left(\sum_i \sum_j d_{ij}\right)} \frac{\sum_i \sum_j d_{ij} \left(h_i - \bar{h}\right)\left(h_j - \bar{h}\right)}{\left(\sum_i (h_i - \bar{h})\right)^2} \qquad (2)$$

where d_{ij} is a spatial weight set to one when *i* and *j* are separated by a desired length scale and otherwise set to zero. Moran's *I* ranges between –1 (inversely correlated) and 1 (perfectly correlated) with 0 being completely uncorrelated. The autocorrelation length scale is defined by the distance over which *I* drops to $1/e$.

To quantify roughness, the sampling interval is important since it needs to be sufficiently small to capture the smallest relevant ice features. From a trafficability perspective, this is roughly the dm-scale, as cm-scale roughness has a minimal impact on travel across the ice surface. The size of the patch over which roughness is evaluated is also critical as it needs to be large enough to be representative of a particular ice regime. For instance, in areas of scattered blocks of rubble, there may be areas of smoother ice in between, where the patch size needs to be large enough to capture the relevant variability.

We utilized a patch size of 10 m ($N = 100$) to calculate both σ and L, which is large enough to capture the relevant variability and small enough to minimize the inclusion of different ice roughness types in one evaluation patch. The 10 m patch size corresponds to the multilook PALSAR resolution cells. *I* is calculated every 0.5 m (shorter intervals did not result in improved results) up to 8 m. Features generally did not correlate with a spacing approaching 8 m. By using 8 m as a cutoff allowed for several correlation estimates to calculate *I* within the 10 m patch size.

Elevation data for each roughness category are sampled from the SDEM along 50 m transects. The transects are used to calculate σ and L for the individual categories and to roughly indicate H_t and H_t/x ratio (see Fig. 2). These values are strictly approximations due to the inevitable impact of the snow cover, which ranged from roughly 5 to 40 cm in depth within the sampled area. We further used these values to construct a schematic linking the feature spacing and feature size to trafficability in a qualitative manner (see Fig. 5).

E. Polarimetric H/α-Decomposition Analysis

For radar signals transmitted in two polarimetric orientations, horizontal and vertical relative to the antenna (H and V), polarimetric SAR evaluates backscatter in the four resultant independent datasets (HH, HV, VH, and VV) [69], [70]. Backscatter strength provides information on the surface type [69]. Polarimetry has previously been shown to be able to indicate different age classes of sea ice, which can be used to estimate ice thickness [51], [71]–[75]. However, to the best of our knowledge, polarimetry has not been applied yet to the derivation of different ice-roughness types. Here, we applied a common classification scheme based on the Wishart distribution [76], [77], an approach that has shown promise over sea ice [78].

We have used PolSARpro 5.0.4 to decompose fully polarimetric PALSAR datasets into entropy *H* and rotation angle α, in accordance with the approach introduced by Cloude and Pottier [79]. *H* and α jointly indicate what kind of scattering mechanism is present. The initial part of the classification effort is based on the assumption that there are three distinctively different scattering mechanisms [80]: Double bounce scattering (high α), surface scattering (low α), and volume scattering ($\alpha \sim 45^\circ$). Low entropy is indicative of a single predominant scattering mechanism, whereas high entropy indicates a combination of scattering mechanisms.

Each pixel can be plotted in the H/α-plane and classified according to 8 predefined classes suggested by Cloude and Pottier [79]. However, in particular, one class was defined too broadly, incorporating varying types of roughness (see Section III-B). We, therefore, used complex Wishart classification [81], [82] to restructure the eight classes, a technique that has shown promise as a tool to map different types of sea ice. However, there is a need for ground truth to properly evaluate the potential of the method [83]. Therefore, we choose to apply a complex Wishart classification and collect the necessary data to evaluate the approach (see Section II-F).

F. DEM Generation From Interferometric SAR

SAR interferometry (InSAR) is a technique that measures phase differences between two SAR scenes acquired from two coherent viewing geometries [84], [85]. The observed phase difference originates from displacement of the scattering surface if measurements were acquired at different times (nonzero temporal baselines) and/or from surface topography if measurements originate from slightly different vantage points (nonzero spatial baselines) [85]. A number of studies have applied long-temporal baseline (>1 day) InSAR to explore deformation of landfast ice [86]–[90] and explored the potential for short-temporal baseline (<1 m) InSAR to investigate more rapid deformation [91]–[93]. However, fewer studies have used bistatic interferometry to calculate topography of sea ice by constructing a DEM [94], but this technique has not been validated yet through ground truthing.

This study utilizes an X-band SAR bistatic image pair acquired on April 10, 2015 at identical times, but from different geometric vantage points. The interferograms were constructed using the Sentinel Toolbox (S1TBX).

Due to the image pair being acquired at identical times, the main contributor for a bistatic phase signal is the topographic phase component. The topographic height difference causing a full phase cycle between two points in a neighborhood can be described as the ambiguity height h_a:

$$h_a = \frac{\lambda R_s \sin\theta}{2B_\perp} \tag{3}$$

in terms of wavelength λ, slant range R_s, off-nadir angle θ, and perpendicular baseline $B_\perp$ [85]. For the image pair used here, h_a is close to 14 m due to $B_\perp$ of 477 m resulting in large ridges being represented by roughly one half-fringe. Since the phase information is directly related to height, it can, therefore, be used to create a DEM (referred to from here as IDEM).

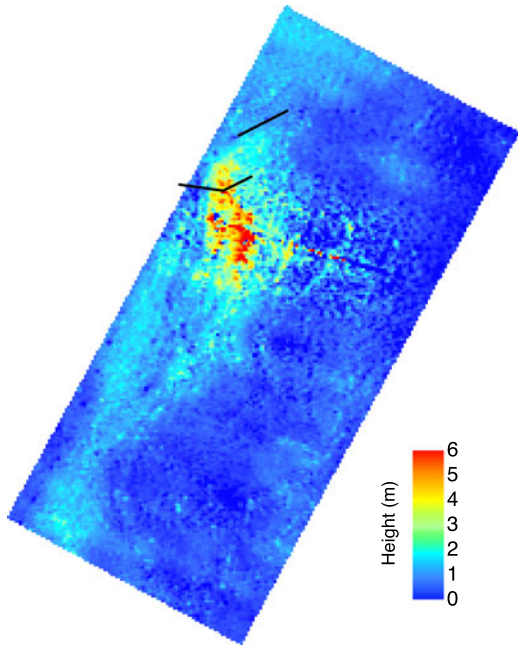

Fig. 6. IDEM (April 10, 2015) indicating good spatial correlation of the ridge. The black lines indicate the location of transects validated using laser survey.

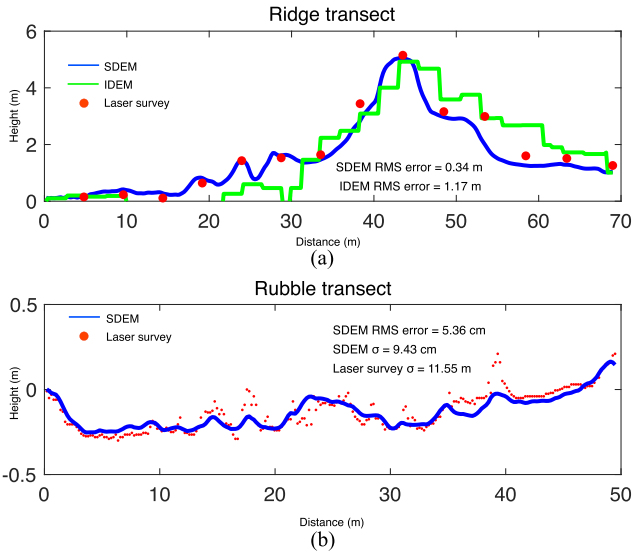

Fig. 7. Transects from a ground-laser survey system compared with the SDEM and IDEM over the ridge (a) and compared with only SDEM in an area of medium rubble (b). The graphs indicate good correlation between both DEMs and ground survey.

III. Results

A. Assessing Ice Topography Through SAR Interferometry

The UAS-acquired image mosaic is used to visually interpret the type of roughness on the ground aided by ground control points [colored rectangles in Fig. 3(a) and (b)]. The numbered triangles and intersecting lines in Fig. 3(b) correspond to the location of individual numbered images and transects in Fig. 2. Superimposing the IDEM on the UAS-acquired image mosaic confirms high spatial correlation between the two data products (see Fig. 6). The height of the SDEM was evaluated along two transects. Transect 1 traversed the ridge, while transect 2 extended across a section of continuous medium rubble (see lines in Fig. 6). The IDEM was only evaluated across transect 1 due to resolution constraints making it incapable of capturing cm-scale roughness of the medium rubble field. Both transects were surveyed *in situ* with laser leveling equipment for quality analysis. The height of the ridge in the IDEM agrees well with both the SDEM and *in situ* survey across transect 1 [see Fig. 7(a)], confirming the ability for InSAR to accurately esti-

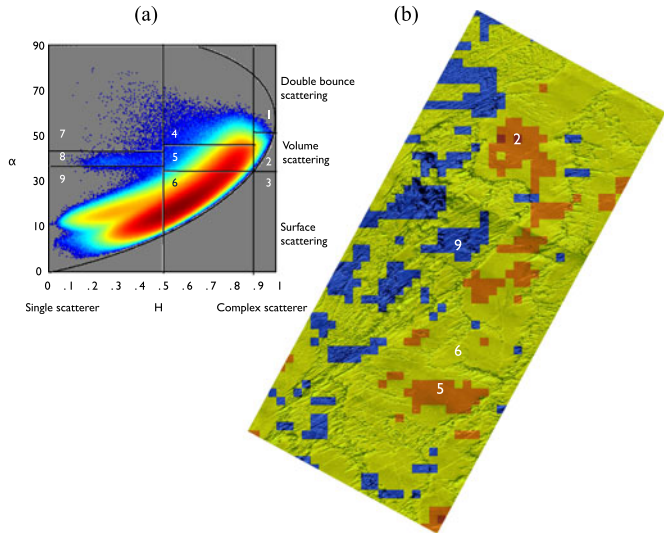

Fig. 8. (a) Each PALSAR pixel plotted into the H/α-plane. Higher concentration of pixels is qualitatively indicated with warmer colors. Rectangular areas correspond to predefined classes. (b) H/α-classification of test area superimposed on the UAS-acquired image mosaic.

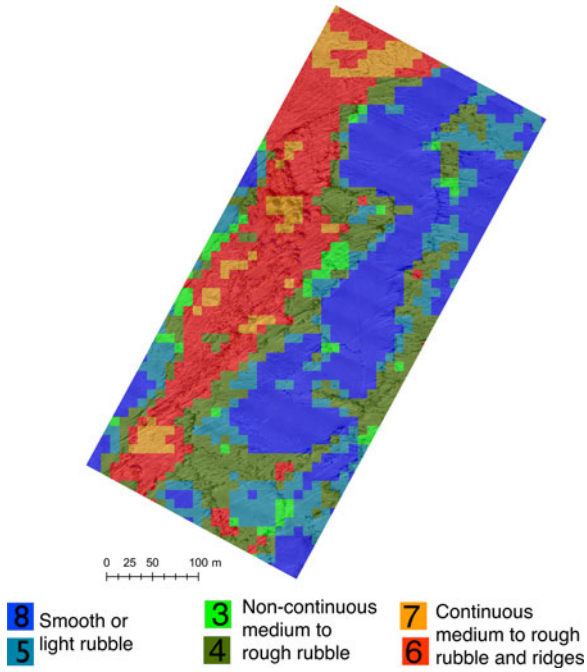

Fig. 9. UAS-acquired image mosaic superimposed on complex Wishart classification, where 6 out of 8 classes appear in the study area. The ridge and areas of continuous rubble are dominated by classes 6 and 7. Regions of rubble adjacent to smoother ice are dominated by classes 3 and 4. Smooth ice and light rubble are dominated by classes 5 and 8.

mate ridge height and thus its potential ability to be used in the trafficability analysis.

The ability to use SfM to assess ice roughness for further evaluation of datasets [e.g., SAR polarimetry (PolSAR)] requires the ability to capture both low-frequency roughness (confirmed along transect 1) as well as high-frequency roughness. The SDEM was, therefore, further evaluated along transect 2 [see Fig. 7(b)]. The *in situ* laser-derived roughness measurements were conducted with a 20 cm sampling interval (sufficient to capture the local roughness), roughly double the SfM sampling interval (11 cm). There is a close match between features in the two datasets indicating the potential for SfM dataset to provide ice roughness data with enough detail for roughness validation and comparison (see Section III-B). Despite the close match between the two datasets, some of the peaks are underestimated in the SDEM. This is due to the high-frequency roughness (low *L*) resulting in some roughness features potentially being reduced by even a slight coregistration offset between the two transects. While the SDEM captures the full roughness frequency spectrum, relative to laser surveying, some of the extreme values of individual roughness features are underestimated. As discussed below, this does not affect the findings from broader, classification- or index-based trafficability assessments.

B. Assessing Ice Roughness Through Polarimetric Classification

An initial H/α decomposition, based on the derivation of entropy H and α, is used to classify each pixel according to predefined rectangular sections in the H/α-plane [see Fig. 8(a)] according to Cloude and Pottier [79]. H and α jointly indicate [see Fig. 8(a)]. Shown spatially over the SfM-derived image mosaic [see Fig. 8(b)], this analysis indicates that

1) smooth areas are dominated by volume scattering (classes 2 and 5),
2) some ridged areas exhibit strong surface scattering (class 9), and
3) the majority of the study area is classified by a combination of backscatter mechanisms with surface scattering dominant (class 6).

This finding, with much of the study area falling into a single class, makes it clear that the outcome of a H/α-decomposition is not suited for an in-depth analysis of ice roughness and trafficability. Hence, we applied a complex Wishart classification [81], [82] to arrive at an optimal segmentation based on data clusters identified through maximum likelihood classification. The Wishart scheme applied here groups an image into eight classes, based on the original H/α classes. Of these, six classes are within the area covered by the SfM DEM (classes 1 and 2 were only found outside of this area). Classes 6 and 7 correspond to the central, highly deformed part of the ridge or continuous rubble, classes 3 and 4 correspond to the outer margins of the ridge/rubble field, class 5 covers areas of light rubble, and class 8 corresponds to wide stretches of smooth ice (see Fig. 9). This preliminary analysis suggests that polarimetric classification holds promise as a source of supporting information to guide trafficability assessments and aid route selection. However, the classification does not provide quantitative information on actual ice roughness, required for an in-depth assessment.

To address this problem, we derived quantitative information on ice roughness from the SDEM, slightly over-sampled to a resolution of 10 cm, i.e., $1/100$ of the polarimetric SAR resolution cell size (10 m). For every SAR resolution cell, we calculated the standard deviation (σ) from the SDEM and superimposed on the same dataset. The spatial distribution of σ

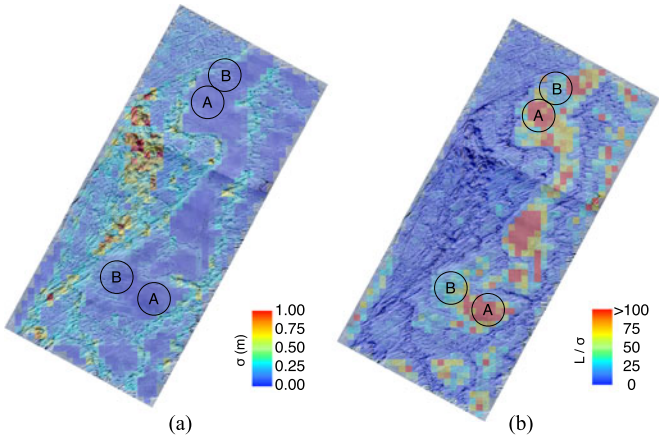

Fig. 10. Standard deviation (σ) of SDEM (a), and autocorrelation length scale divided by standard deviation (L/σ) (b), calculated over 100 × 100 pixels. The UAS-acquired image mosaic is superimposed on each plot. Circles indicate areas of similar σ-values, but with different roughness and L/σ-values between A and B.

is structured as expected, with low values over smooth ice and higher values for rough ice [see Fig. 10(a)]. However, σ by itself is not sufficient to distinguish between different spatial roughness scales. Hence, L was derived to enhance trafficability assessments. By dividing L by σ [see Fig. 10(b)], areas of high L associated with smooth ice will have a high L/σ ratio, whereas high L in conjunction with rough or ridged ice (in the case of correlation between large roughness features) will result in lower L/σ ratios. L/σ is low for both ridges and rubble and thus a good discriminator between consistently smooth ice [high L/σ—see regions marked A in Fig. 10(b)] and smooth ice with interspersed roughness features [lower L/σ—see regions marked B in Fig. 10(b)]. PDFs of σ and L/σ are plotted for all six Wishart classes in Fig. 11(a) and (b).

With the exception of the classes 3 and 4 at the margins of deformed ice, it is clear that each class represents slightly different PDFs, in particular, in terms of the presence of near-zero values and the length of the tail. This difference is rooted in the fact that differences in roughness impact the polarimetric signal. Class 8 favors high L/σ values, while class 5 contains some higher L/σ values as well. Classes 3 and 4, corresponding to the margins of deformed areas, mostly lack low and high L/σ ratios. Ridged ice (classes 6 and 7) is represented by the lowest values in the study area. There are, however, large overlaps between the PDF's due to different types of roughness being represented in many pixels and the SAR signal being sensitive to small-scale ice properties independent of surface roughness. Even so, it is clear that small-scale surface properties must remain partly consistent throughout the major areas of rubble and smooth ice enabling a discrimination of the different roughness areas (see Fig. 9) despite the strong PDF overlap.

C. Assessing Ice Trafficability for Community Ice Trail Areas

Based on the promising results for InSAR (see Section III-A) and complex Wishart classification (see Section III-B) to evaluate ice roughness, we can now evaluate the relative roughness and hence trafficability of different subregions of our study area. To achieve this, we utilize trails as placed by Iñupiaq ice experts at Utqiaġvik (see Fig. 1). In addition to InSAR and Pol-SAR, we also utilized single-channel X- and L-band SAR from TerraSAR-X and ALOS PALSAR-2, respectively, due to the strong relationship between surface roughness and the backscatter coefficient.

SAR products are sampled every meter along the trails and the linear endpoint connectors. Resulting probability density functions are displayed in Fig. 12 of X-band SAR digital numbers (DN) from the multilook ground range detected product (a), X-band InSAR-derived relative height (b), and L-band complex Wishart classification (c). From the comparison, it is clear that the trails as placed by Iñupiaq ice experts (red) favor both lower SAR backscatter values and lower height values compared to the endpoint connectors (blue). In addition, class 8 and less so class 5 from the complex Wishart classification appear to be favored for trail routing. This is to be expected from the analysis in Section III-B indicating that these classes correspond to smooth ice or light rubble.

Using information from the PDFs shown in Fig. 12(a)-(c), we calculate the relative likelihood of a particular pixel value representing a preferred surface type for ice trail construction. For every pixel [*i,k*] and SAR-based product (i.e., interferometric height, polarimetric class, or X-band amplitude values), we calculate $T_n[i,k]$, a measure describing whether the pixel is favored ($T_n > 0.5$) or not ($T_n < 0.5$) in terms of trafficability:

$$T_n\,[i,k] = \frac{p_t}{p_e + p_t}. \tag{4}$$

Every pixel belongs to a single bin in all three PDFs where p_t and p_e are the probability of a trail and endpoint connector occupying the same bin, respectively. $T_{\rm n}$ is the trafficability determined by a specific SAR-based method, with n = I, P, or X indicating use of interferometric height, polarimetric classes, or X-band DN values. T_n ranges from 0 (no trail segment falls in the respective bin, hence low trafficability) to roughly 0.8 (trail segments fall in the respective bin four times as frequent as endpoint connectors), with a hypothetical limit of 1. It is worth noting that this range is subject to change with different roughness regimes. For instance, for smoother ice, endpoint connectors will more frequently occupy bins similar to trails narrowing the range of T_n values. Trafficability for bins on the left side of the histograms in Fig. 12(a) and (b) is set to 1 and on the right-side set to 0. We define the trafficability $T_{\rm IPX}$ utilizing interferometric ($T_{\rm I}$), polarimetric ($T_{\rm P}$), and X-band DN values ($T_{\rm X}$) as

$$T_{\rm IPX} = T_I \cdot T_P \cdot T_X. \tag{5}$$

$T_{\rm IPX}$ is assessed for both the trails and the endpoint connectors in a similar manner using PDFs and is displayed in Fig. 12(d). The distribution shows, as expected, that trail routing favors areas of higher trafficability. The combination of *T*-values obtained through three different methods amplifies the spread of values, and hence likely increases accuracy of the compound trafficability estimate $T_{\rm IPX}$ compared to individual *T* values.

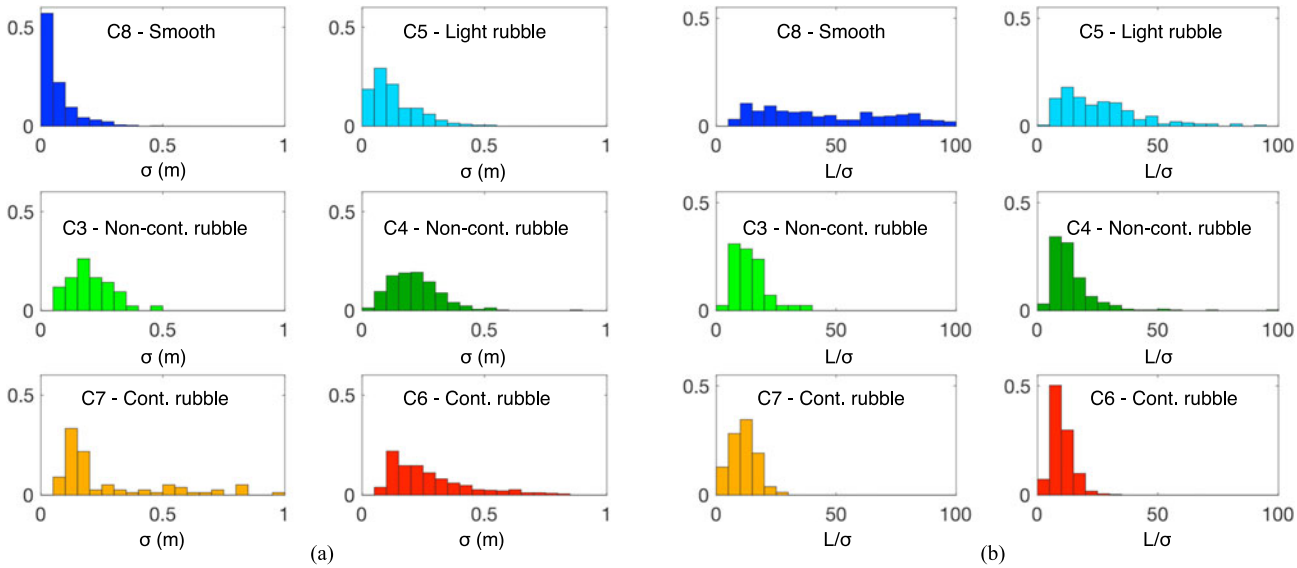

Fig. 11. PDF of σ (a) and L/σ (b) within their respective polarimetric class. L/σ for class 8 is cut off by 100, but includes values above 200 indicated in Fig. 10(b).

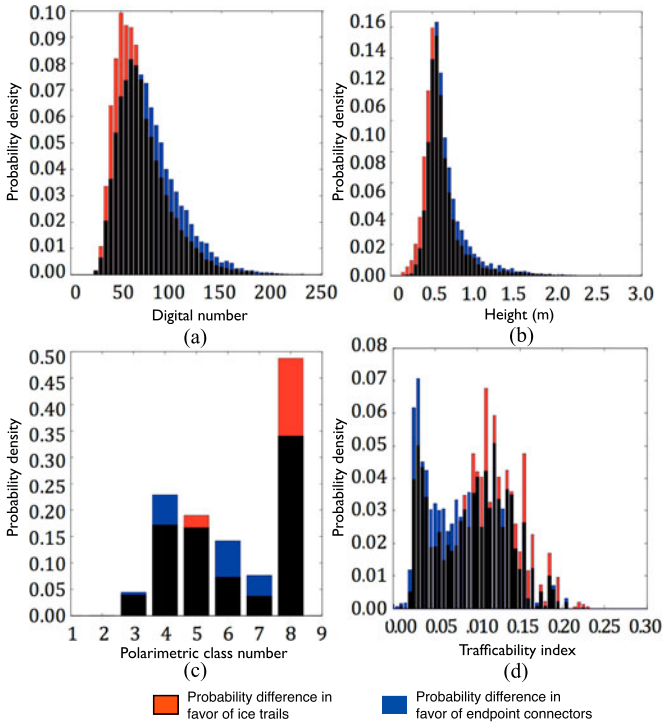

Fig. 12. PDF of values under ice trails (shown in red) superimposed on PDFs of endpoint connectors (blue) with overlapping bars in black for X-band DN image values (a), X-band interferometric height (b), and complex Wishart classification (c). The calculated trafficability PDF utilizing PDF (a)–(c) is displayed in (d) (T_{IPX}).

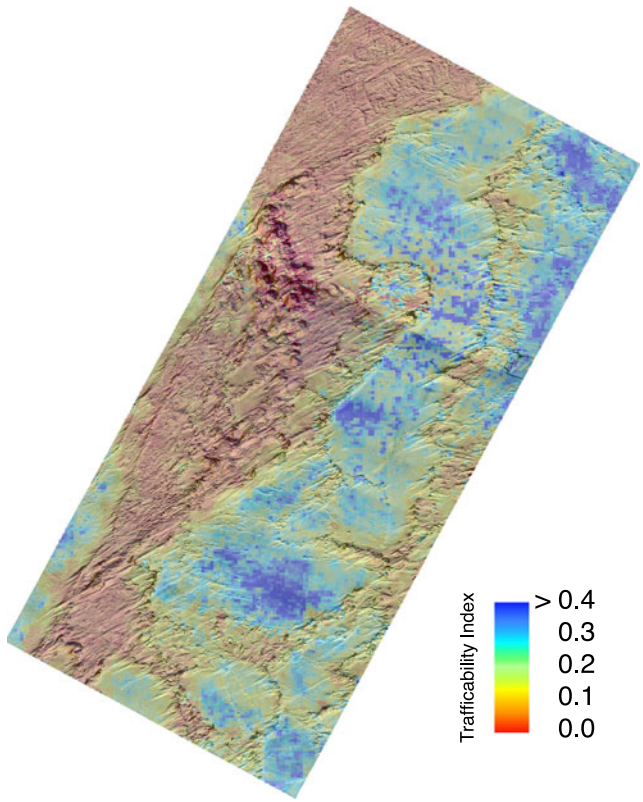

Fig. 13. Trafficability index superimposed on the UAS-acquired image mosaic.

The trafficability index T_{IPX} retains the resolution of the highest-resolution SAR product, in this case 2.35 m, which is the multilook resolution of T_{I}. Over the extent of the SfM scene, the magnitude of T_{IPX} anticorrelates highly with the ridge (see Fig. 13). Low values are shown in red, which cover the ridge and the areas difficult or impossible to traverse. High values shown as blue and green over smooth or light rubble areas classify these as trafficable. Yellow, midrange values cover border regions between smooth and rough ice.

D. Route Selection Based on Cost-Index Estimates

Utilizing multiple SAR products, it is possible to create a large-scale trafficability assessment that can help guide decision

TABLE IV
COSTS OF DIFFERENT TRANSPORTATION/CONSTRUCTION PURPOSES AND ICE ROUGHNESS TYPES

Ice roughness type	Cost of ice trail (IT)	Cost of ice road (IR)	Cost of ice scouting (IS)	Trafficability at control points
Smooth	0.2	4	0.01	0.231
Light rubble	1	5	0.01	0.183
Medium rubble	2	6	0.01	0.162
Rough rubble	4	9	10	0.056
Ridge	6	10	10	0

making for ice road or trail development. An important question to explore is whether data such as those analyzed here allow for the determination of an optimal trail route. Such an evaluation requires a measure of relevance of different roughness categories for the specific trail or ice user, which will largely depend on the mode of transportation, level of ice construction or modification needed, crew size, and related factors.

The trafficability assessment (see Section III-C) is used to determine an idealized route and to identify optimal data combinations for routing purposes. T_{IPX} values for five control points spanning all five roughness classes [points 15, 8, 11, 12, and 2 in Fig. 4(a)] are listed in the last column of Table IV. Depending on the mode of transportation, these different roughness classes are associated with different costs or penalty values, which can be estimated in both workload, price of construction, or time and will depend on available resources and the trail surface end state needed (e.g., level of smoothness). An example of how this can be calculated can be found in the study Spencer *et al*. [33]. Here, we demonstrate the general approach for arbitrary cost values (see Table IV), focusing on relative, not absolute magnitudes.

Every derived trafficability value is linearly interpolated to a cost value for three different use scenarios:

1) ice trail construction by local communities utilizing snowmobiles,
2) construction of an ice road by a local government or industry capable of supporting construction vehicle and car traffic, and
3) ice scouting with snowmobiles without any ice modification or construction.

The relative cost values between roughness classes are different for the three use scenarios (see Table IV). The cost associated with each use scenario depends on a number of factors relevant along the optimum path, such as height thresholds that determine whether a ridge can be traversed. Mostly, the routing will be constrained by the cost/benefit ratio associated with traversing rough areas for the benefit of a short path. Following is a justification for the assigned cost values.

For ice trails such as those created at Utqiaġvik by the local population, rougher stretches frequently involve cutting of paths and infilling with ice blocks cut and shaped to smooth out the trail, so as to allow towing of large sleds and boats through the ice by snowmobile. Several crews may choose to collaborate on breaking through the roughest sections. Since all labor is by hand, it is critical for existing smooth areas to be utilized wherever possible. At the same time, the trail should not be too long, allowing for quick evacuation in a case of emergency. Smooth ice is, therefore, given a small cost (0.2), but not zero, ensuring a small penalty for a long trail. From smooth ice, cost is set to increase up to 6 for ice difficult or impossible to navigate where substantial construction is needed. For an ice road, we place a substantially larger penalty on smooth ice. For intensive road use during the season, reducing distance traveled via road becomes important. Also, in case of an industry ice road, substantial work is associated with road construction (e.g., artificial thickening of the ice) across even smooth areas reducing differences in cost for different ice types (roughest ice is set to only 2.5 times the penalty of smooth ice for ice road versus 30 times for ice trail). For over-ice travel by snowmobile for the purposes of ice scouting in search of a navigable path, i.e., not associated with repeated use of trails and without any ice modification, we are selecting a near binary cost assignment. For ice that is fairly easily traversable, the cost is set to near zero, and for ice that can be difficult or potentially impossible to navigate, the cost is set to ten. This will allow for a long travel route circumnavigating areas of rough ice.

To evaluate the proposed approach, we compared the most cost-effective routes based on the conversion outlined above with constructed trails. Two trail segments (of the three enclosed in the red rectangle in Fig. 1) were assessed, with the eastern trail (A) considered in its entirety and the western trail (B) considered from the start at the shore to the edge of the TanDEM-X scene. The trafficability index validated in Fig. 13 is displayed for the area in Fig. 14(a) with ice trails indicated in blue. Using the cost assignments from Table IV, lowest cost paths are calculated for a hypothetical ice trail (IT) (red), ice road (IR) (yellow), and ice scouting path (IS) (green). The expectation is that the trails created by local experts after considerable scouting and tracking of ice conditions over the course of the season are close to optimal, with some dependence on the experience of the crew [3]. Hence, any method that is able to closely match actual trail routing holds promise to help determine trail or ice road construction in operational settings.

For trail A [eastern trail in Fig. 12(a)], the trail (blue) follows the edge of an area of rubble ice to the west and through a small ridge [indicated by "1" in Fig. 14(a)] of lower trafficability. From there, the trail stays on a stretch of newer ice outside of the deformed shear zone ("2"). The trail follows this low-resistance route and makes a turn ("3") heading almost perpendicular to the ridges to minimize the distance traversed in the ridged areas. The IT (red) follows the general path of the actual trail and makes the two major turns ("1" and "3") at the same locations. Only toward the end, there is a small deviation. The IR prediction (yellow) takes a straighter route through a passage of high trafficability (but lower than the path of the actual trail) to reduce the cost of added distance. The IR continues up the same smooth refrozen lead ("2") and makes a less sharp turn to save on distance for the second turn. IS (green), the smoothest route, hugs the shore, part of it likely on bottomfast ice, before looping around in a detour avoiding some of the light to medium rubble and continuing up the smooth frozen lead. For the last section, IS and IT follow the same path.

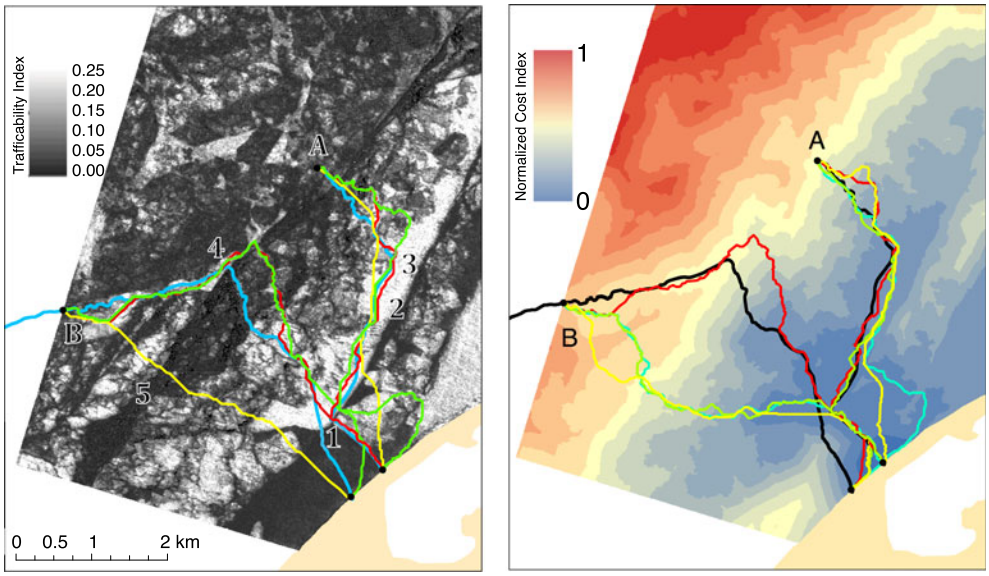

(a) (b)

Fig. 14. (a) Trafficability index (T_{IPX}) surrounding two ice trails (blue lines) near Utqiaġvik. Remaining lines represent lowest cost paths for construction of an ice trail (red) and an ice road (yellow) and ice scouting (green). (b) Normalized cost of ice trail construction from starting point of trail A to any other location on the map. Colored lines represent optimal trails calculated using a combination of SAR products: $\mathrm{IT}_{\mathrm{IPX}}$ (red), $\mathrm{IT}_{\mathrm{PX}}$ (cyan), IT_{X} (green), and IT_{L} (yellow).

Trail B (blue) does not take advantage of the smooth frozen lead, but tracks a straighter path out from the coast. The trail finds a relatively efficient route through the extensively ridged area. This trail was particularly difficult to construct through this area and the trail work ceased for some time before it was completed (Unpublished trail surveys, 2015). On the other side of the rough ice ("4"), the trail follows a refrozen lead taking advantage of the smooth ice in this passage. IS and IT are following similar paths attempting to avoid as much of the rubble ice in the beginning of the trail and are passing through "1." This is different from the actual trail and is linked to the presence of snow at the time of trail building further discussed in Section IV-D. IT and IS deviate approaching the severely ridged area and choosing to enter the refrozen lead further up than "4." This passage crosses lower elevation ridges in an area of higher trafficability (T_{IPX}). The IR follows a relatively straight path (passing just north of the narrowest part of the ridge "5") with small deviations to take advantage of smoother areas.

E. Optimal Path Routes and Sensitivity to Different SAR-Derived Data Products

By utilizing the trafficability index T_{IPX} to cost conversion for IT outlined in Section III-D, we can calculate the cost from a given starting point to any other location. Here, we perform this calculation from the starting point of trail A. The resulting normalized cost index map [see Fig. 14(b)] allows us to identify different directions of low cost, which may help guide routing of trails. The starting point of trail B is close to that of trail A; hence, the cost index maps for the two starting points are nearly identical (not shown). To address the relevance of each individual SAR product in the calculation of an optimal trail, we repeated the steps outlined in Sections III-C and III-D for IT [see Fig. 14(b)] based on X-band SAR backscatter and Pol-SAR (excluding InSAR) (T_{PX}), and only X-band backscatter (T_{X}). We also tested the dependence on wavelength frequency by applying L-band backscatter (T_{L}). All products were resampled to the lowest resolution of L-band SAR (multilooked to 10×10 m).

The calculated optimal trails are again compared to trails A and B (black). The trail calculated using T_{IPX} ($\mathrm{IT}_{\mathrm{TPX}}$) is displayed in red, $\mathrm{IT}_{\mathrm{PX}}$ in cyan, IT_{X} in green, and IT_{L} in yellow. For trail A, all calculated IT follows the general path, with an exception of the starting direction in $\mathrm{IT}_{\mathrm{PX}}$ and IT_{L}. These two products are not sensitive to elevation and are either exclusively based on or more strongly impacted by L-band than $\mathrm{IT}_{\mathrm{IPX}}$ (IT_{L} and $\mathrm{IT}_{\mathrm{PX}}$,respectively). L-band is sensitive to roughness on scales of 20–30 cm and X-band on scales of 1–5 cm. With L-band being less sensitive to smaller than dm-scale roughness features, it is possible that these routes cross light rubble features, while the other approaches choose alternate paths.

There is a larger difference between the trail products for trail B. Initially, the optimum trails take the same path, but here, $\mathrm{IT}_{\mathrm{IPX}}$ is the only trail that follows the general path of trail B by crossing the ridge close to "4" and utilize the refrozen lead. By not utilizing InSAR-derived height, the trails take a more direct path crossing what is likely more topographically challenging terrain. Toward the end, IT_{L} deviates, choosing a path through an area of likely small-scale roughness that is underrepresented in the L-band signal, but shows up more clearly in X-band.

IV. Discussion

Our analysis demonstrates that the remote sensing tools employed here, specifically SAR polarimetry, backscatter amplitude analysis, and InSAR-derived DEM, support detailed evaluation of sea-ice trafficability for different applications. The approach developed here can help determine favorable paths, in particular, if combined with application-specific parameterization of trail cost. Cost maps, such as featured in Fig. 14(b), can

be used to identify least costly options, but also identify several possible options for ice travel. The latter are particularly relevant in the following contexts:

1) Routing of seasonal ice trails by coastal communities for hunting and travel. This approach may help improve safety and efficiency of trail construction. For instance, Fig. 14(b) demonstrates that trail A, where rough ice led to termination of trail breaking before the ice edge was reached, would have resulted in high costs to complete.
2) Determine optimal travel paths for a range of uses such as scientific research and military operations.
3) Routing of ice roads through roughness types compatible with a specific trail construction method.
4) Delineation of evacuation routes away from offshore infrastructure and installations.
5) Temporary logistical operations such as stretching of fuel lines across landfast ice between refueling barges and coastal communities.
6) Identification of potential on-ice aircraft landing strips.

A. Benefits of InSAR-Derived Height and Polarimetric Information in Trafficability Analysis

We need to consider the relevance of the source data used to calculate roughness and trafficability for ice trail or road routing assessments—in particular, whether DEM products require use of InSAR data for sufficient accuracy. Polarimetric and backscatter amplitude data have the advantage that they do not need to be acquired by twin constellations such as TanDEM-X. Unless requested specifically, single-pass interferometric products are rarely acquired routinely and should be obtained in bistatic mode since even a few seconds of temporal baseline can result in vertical shifts through ocean interaction to produce a phase signal interfering with the height analysis [92]. A more effective way of acquiring bistatic data is from airborne platforms. Interferometry provides important, nonredundant information in the context of trafficability assessments, yielding a predicted trail route most closely tracking that of the actual trail [see Fig. 14(b)]. Trafficability is significantly constrained by ridge height [56] such that the promising results obtained from InSAR highlight the need for better coverage by twin constellation InSAR systems in the future.

Fully polarimetric acquisitions are much less common than single- or dual-polarimetric acquisitions, and it is thus beneficial to consider the actual need for polarimetric data. Polarimetric classification seems effective in delineating certain roughness types (e.g., rubble from smoother ice), but we find that single-channel L-band alone also produces good results under certain parameter constraints. For example, using a nonrestrictive path length and only high costs for severe roughness (IS), the predicted travel path based on L-band data alone closely captures the actual ice trail route (not shown). Hence, out of all factors considered, accurate representation of differential trail costs is most critical for optimal trail route prediction. More research is needed to understand the full benefits of polarimetric data for trafficability analysis (e.g., use of other classification approaches and different combinations of datasets). However, based on our results, we speculate whether a combination of single-channel L- and X-band will provide close to equal accuracy to polarimetric products and thus be superior due to higher data availability and much lower computational cost.

B. Sensitivity to Radar Wavelength and Resolution

Throughout this work, we have identified different classes and types of roughness, each associated with different features and length scales. Hence, sensor resolution and wavelength play an important role in the detection of surface obstacles, with little contribution to backscatter by feature sizes well below sensor wavelength. Trail routes obtained from X-band and L-band data differ mostly only in areas of small-scale roughness.

The larger wavelength of L-band (24 cm), compared to X-band (3 cm), makes it less sensitive to smaller than dm-scale roughness, with little impact on assessments for most modes of transportation. L-band sensors such as PALSAR-2 are, therefore, more valuable SAR tools for such applications and in our analysis capture and integrate both the smooth refrozen lead and the severe ridging into an optimal trail route. X-band may be more appropriate for identification of potential aircraft landing strips where even cm-scale roughness can be critical unless smoothed by snow [30]. However, an added benefit of X-band is its higher spatial resolution, enabling identification of narrow passageways between ridged areas. X-band backscatter is also able to better distinguish between roughness such as rubble close to shore (lower backscatter) versus ridges further offshore (higher backscatter). A combination of L- and X-band products is therefore likely optimal for trail routing.

SAR product grid size may impact the extent of multilook acquisition and processing of scenes at full resolution. For the comparison in Section III-E, we undersampled all X-band data to the coarser 10 m $\times$ 10 m grid. Low-cost paths calculated for X-band on this coarse grid differ little from routes derived for a 2.75 m $\times$ 2.75 m grid, suggesting low sensitivity of this approach to grid size.

C. Cost Assignment

It is apparent that calculations of optimal ice trails depend heavily on the cost assigned to individual ice types. Costs estimated in this study are based on a heuristic approach that takes into consideration differences between ice road or trail uses and is informed by cost assessments in other settings. Cost elements such as construction effort, time, workload, and safety were considered. More accurate cost estimates reflecting local conditions could be obtained through Monte Carlo simulations. Routes predicted for a large ensemble of trails with slightly altered cost values will provide estimates of the sensitivity of trail routing on cost models and help arrive at appropriate cost functions that reflect the full set of constraints governing trail or IR construction and use. For such an approach, a larger validation dataset can help identify biases in road or trail routes based on factors other than roughness.

We have compared calculated low-cost trails with actual trails to evaluate the methodology, assuming that the actual trail is an efficient route. However, more efficient routes may exist. This could be due to 1) routing priorities other than roughness avoidance, such as ice stability, proximity to town, etc., and 2) the

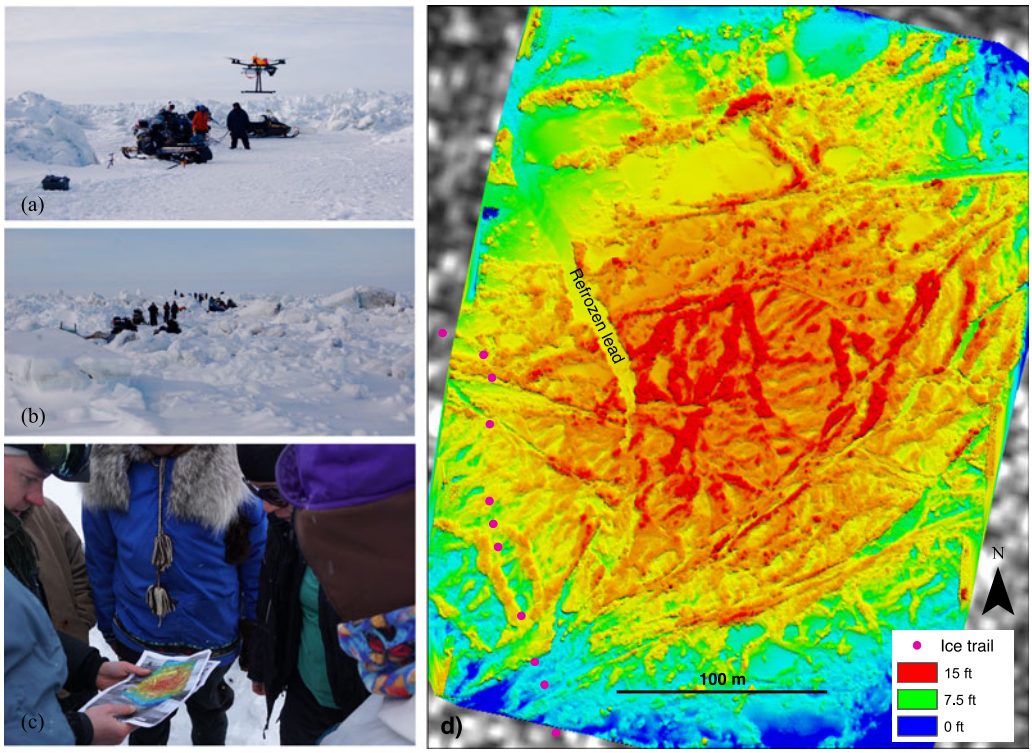

Fig. 15. (a) Launching hexacopter UAS next to trail surveying crews on April 11, 2015. (b) Crew members on the ice trail observing the UAS flying overhead. (c) Discussion of data products out on the trail with crew members. (d) DEM product shared with community members working on ice trail on April 12, 2015. Green colors represent medium topography (roughly 2 m), while red indicates topography up to roughly 5 m. Scale bar is in feet to conform with local use.

trail building crew not being able to fully assess the roughness in alternate areas. Ideally, different trail priorities should be separated to enable trail optimization for different cost combinations, such as cost-effectiveness or safety. Separating the cost functions would also allow for considering only relevant costs in a specific scenario, which is important when expanding this approach to different modes of transportation or ice use scenarios.

D. Additional Trafficability Analysis Constraints

As outlined in Section III-C, trafficability has been calculated utilizing a set amount of existing ice trails that are located within the area covered by remote sensing data. For the interferometric data and analysis in particular, this corresponds to a small number of trail segments. Consequently, trafficability calculations drawing on the PDFs shown in Fig. 12 are constrained by a comparatively small set of source data. Nevertheless, even for a low number of trail segments, the method appears to perform well, capturing actual trafficability as well as predicting optimal trails [see Fig. 14(a) and (b)]. This statistical approach to calculate trafficability will be further improved as more remote sensing datasets become available and future trails are mapped.

Sea ice travel greatly depends on the presence of snow and in some communities, ice travel often has to wait until after snowfall [24]. Snow greatly affects the trafficability of rubble and ridged ice leading to some of the discrepancies between actual and predicted optimal trails in this analysis. For instance, for the first section of trail B, none of the IT or IS followed the actual trail, but chose the shortest path out of this area of low trafficability. This area was close to nontrafficable early in the season, but by the time the trail was made, snow covered the rubble to such a degree as to allow effortless traversing. SAR signals are not significantly affected by the presence of dry snow, such that the impact of snow cover on changing inherent ice roughness and trafficability is more difficult to estimate in regions where this is of relevance. However, in locations of wet snow and ice cover such assessments of the impact on the SAR signal, in particular, in X-band, are to be considered.

There are, however, methods that can help account for snow cover in the T_{IPX} estimates. The rubble field at the start of trail B appears with variable height in the IDEM (not shown) resulting in lower than 0.5 trafficability calculated from the interferometric height [see Fig. 12(b)], but if the relative elevation was reduced by 20 cm (approximate snow depth), the majority of the area would exhibit a trafficability above 0.5 and hence contribute to higher rather than lower trafficability scores. With evidence for substantial snowfall, e.g., from time series of automated snow depth measurements (such as available at Utqiaġvik), one possibility is to classify heights below a snow-depth-dependent threshold as trafficable. Snow cover also inevitably impacts the roughness calculations in Fig. 11(a) and (b) since SfM does not penetrate the snow like SAR does.

E. Potential Use of UAS-Based Trafficability Analysis

In addition to acquiring a UAS-based SfM-derived DEM for SAR validation purposes, we also explored the possibility for UAS surveys in support of ice use. Leading up to the trail construction season in Utqiaġvik, we communicated with community leaders and members of the Barrow Whaling Captains Association to determine what scientific efforts could aid trail

construction and safety on the ice. We found a general community interest in products that could determine ice roughness and associated support for surveying a relevant section of very rough sea ice around trail construction efforts. On April 11, 2015, we set up a UAS launch site on the side of a trail (see Fig. 1) by what was at the time the current trail endpoint. We then launched [see Fig. 15(a)] and surveyed the ice immediately ahead of the construction crews [see Fig. 15(b)]. Within 24 h, we returned to the trail and presented crewmembers with a DEM processed in the field [see Fig. 15(c)]. The map highlighted large ridges in red and allowed for identification of important features for crewmembers to avoid such as a refrozen lead [see Fig. 15(d)], where fractures may occur [95]. The final trail ended up steering clear of some of the most severe roughness and the refrozen lead [purple dots in Fig. 15(d)].

The potential of UAS-based tactical surveying and trafficability analysis through SfM became clear through this work. Following is a selection of some of the findings arrived at throughout the survey effort:

1) UAS-based systems, such as the hexacopter used here, have a lower impact visually and in terms of noise than airplanes, hence result in reduced disturbance of marine mammals and subsistence activities.
2) Extreme Arctic conditions can create narrow operating windows for operations posing a challenge to operational use. We found it difficult to operate UASs at temperatures below roughly –20 °C at which point, finger dexterity for the controller becomes reduced. Also, the hexacopter with its full payload was only able to operate up to roughly 5 $m \cdot s^{-1}$ winds, reducing the operating window.
3) By using the described hexacopter, we were able to demonstrate the potential of using a UAS-based surveying approach, but a fixed-wing UAS is needed to survey the roughly 30 km coastline used for trail construction. A fixed-wing system may also reduce the concerns in (2).
4) The way we displayed the DEM [see Fig. 15(d)] was not optimal for effectively communicating ice topography to the local population and more work needs to be done to explore best practices for visualizations presented to community members.
5) Long-term impacts of use of UAS in subsistence areas need to be considered such as direct and indirect consequences on subsistence activities including its cultural and educational components.

V. Conclusion

This work represents one of the first studies of sea ice trafficability using remotely sensed data drawing upon multiple methods developed within the last decade or two, but which have not been applied to sea ice. The acquisition of high-resolution imagery using UAS allowed us to both evaluate SfM over sea ice and validate other approaches such as SAR polarimetry and interferometry. We demonstrate here that cm-scale SfM is capable of distinguishing between different types of roughness relating to ice trafficability. Also, SfM has provided a deeper understanding of relevant polarimetric scattering mechanisms and improved discrimination between different roughness classes that are unique in the classification scheme. We have demonstrated that roughness, from a trafficability perspective, can be assessed from SAR data alone. A combination of interferometry, polarimetry, and the backscatter coefficient provides an optimal assessment of trafficability through an evaluation of both scattering mechanisms and surface height of the scattering medium.

The combination of remote sensing data and ice trail surveys supported the development of a trafficability index and calculation of optimal travel routes. This method is most accurate when including bistatic interferometry to assess ridge heights. However, backscatter data alone have shown promise as a tool to assess trafficability, and in particular, if combining different frequencies such as X- and L-band. These findings suggest that large-scale assessments of landfast ice trafficability at pan-Arctic scales are possible due to the wide availability of SAR backscatter cross-section data. A large-scale or pan-Arctic assessment of trafficability and analysis of how trafficability has changed over the last decade can potentially lead to important new insight into the effects of climate change on both communities and industry. Large-scale assessments may improve ice route selection making ice travel more cost-effective and possibly counter negative effects of rougher ice and a shorter landfast ice season.

In this study, we defined trafficability as the efficiency and required resources of traveling across ice, which mostly depends on surface conditions. However, trafficability can also be defined more broadly incorporating elements related to safety as well as a larger set of objectives for travel. It is likely that applying an additional set of remote sensing techniques to construct a trafficability assessment could accommodate a broader trafficability definition. Also, it is clear here that an important aspect of trafficability is not only the general roughness of the ice cover, but perhaps, more importantly, the presence and connectivity of smooth trafficable areas. An important next step will be to develop a metric for this connectivity and determine how it links to overall trafficability.

Optimal travel routes depend on the mode of transportation and priorities with respect to path length versus roughness types. More work needs to be done to understand the exact specifications of different modes of transportation and their limitations in terms of ice roughness. The strategy outlined in this paper, utilizing multiple remote sensing products to approach a trafficability assessment, does not limit itself to sea ice, but can potentially be utilized on any surface and mode of transportation.

Acknowledgment

The authors would like to thank the community of Utqiaġvik and the Barrow Whaling Captains Association for their generosity allowing UAS flights in subsistence hunting areas. A special thanks to whaling captain H. Brower Jr. who provided valuable guidance during planning and execution of the UAS mission surveying his crew's trail. The authors thank the North Slope Borough Department of Wildlife Management for guidance and in-kind support and acknowledge UIC Science for providing logistic support making this project possible. The au-

thors would like to thank P. Hickman at the Geographical Network of Alaska for programming support. A great thank you to J. Nicoll at the Alaska Satellite Facility for guidance relating to polarimetric analysis. Satellite data were generously provided by the Japanese Space Agency JAXA through a data grant (ALOS PI 1493), the Alaska Satellite Facility, and by the German Aerospace Center (DLR) (TanDEM-X and TerraSAR-X) through science proposals (COA_1987 and XTI_GLAC6921). The authors further acknowledge two anonymous reviewers who provided valuable feedback leading to an improved paper.

REFERENCES

[1] H. Eicken, A. L. Lovecraft, and M. L. Druckenmiller, "Sea-ice system services: A framework to help identify and meet information needs relevant for arctic observing networks," *Arctic*, vol. 62, pp. 119–136, Jun. 2009.

[2] C. Aporta, "Routes, trails and tracks: Trail breaking among the Inuit of Igloolik," *Études/Inuit/Studies*, vol. 28, pp. 9–38, 2004.

[3] M. L. Druckenmiller, H. Eicken, J. C. George, and L. Brower, "Trails to the whale: Reflections of change and choice on an Iñupiat icescape at Barrow, Alaska," *Polar Geography*, vol. 36, pp. 5–29, 2013.

[4] M. Jaervik, "Road on the sea," in *Proc. PIARC XII Int. Winter Roads Congr.*, Torino, 2006.

[5] G. J. Laidler *et al.*, "Travelling and hunting in a changing Arctic: Assessing Inuit vulnerability to sea ice change in Igloolik, Nunavut," *Clim. Change*, vol. 94, pp. 363–397, 2009.

[6] M. Nuttall, F. Berkes, B. Forbes, G. Kofinas, T. Vlassova, and G. Wenzel, "Hunting, herding, fishing and gathering: Indigenous peoples and renewable resource use in the Arctic," in *Arctic Climate Impact Assessment*. Cambridge, U.K.: Cambridge Univ. Press, 2005, pp. 649–690.

[7] R. Potter, J. Walden, and R. Haspel, "Design and construction of sea ice roads in the Alaskan Beaufort sea," in *Proc. Offshore Technol. Conf.*, Houston, TX, 1981, pp. 135–140.

[8] E. K. Bashaw, J. Drage, S. K. Lewis, and C. Billings, "Applied Ice engineering for exploring arctic natural resources," in *Proc. 10th Int. Symp. Cold Regions Develop.*, 2013, pp. 308–319.

[9] A. G. Krieger, G. N. Kidd, and D. A. Cocking, "Northstar drilling-delivering the first arctic offshore development," *SPE Drilling Completion*, vol. 18, pp. 188–193, 2003.

[10] D. Mesher, S. Proskin, and E. Madsen, "Ice road assessment, modeling and management," in *Proc. 7th Int. Conf. Manag. Pavement Assets*, Calgary, AB, 2008, p. 11.

[11] V. Selyuzhenok, T. Krumpen, A. Mahoney, M. Janout, and R. Gerdes, "Seasonal and interannual variability of fast ice extent in the southeastern Laptev sea between 1999 and 2013," *J. Geophys. Res., Oceans*, vol. 120, pp. 7791–7806, 2015.

[12] A. Mahoney, H. Eicken, A. G. Gaylord, and R. Gens, "Landfast sea ice extent in the Chukchi and Beaufort seas: The annual cycle and decadal variability," *Cold Regions Sci. Technol.*, vol. 103, pp. 41–56, Jul. 2014.

[13] J. C. Stroeve, M. C. Serreze, M. M. Holland, J. E. Kay, J. Malanik, and A. P. Barrett, "The Arctic's rapidly shrinking sea ice cover: A research synthesis," *Clim. Change*, vol. 110, pp. 1005–1027, Feb. 2012.

[14] J. C. Comiso and D. K. Hall, "Climate trends in the Arctic as observed from space," *Wiley Interdiscip. Rev., Clim. Change*, vol. 5, pp. 389–409, 2014.

[15] W. N. Meier *et al.*, "Arctic sea ice in transformation: A review of recent observed changes and impacts on biology and human activity," *Rev. Geophys.*, vol. 52, pp. 185–217, 2014.

[16] AMAP, "Snow, water, ice and permafrost in the Arctic (SWIPA): Climate change and the cryosphere," Oslo, Norway, 2011.

[17] H. Eicken and A. Lovecraft, *Planning for Northern Futures: Lessons From Social-Ecological Change in the Alaska Region*. Fairbanks, AK, USA: Univ. Alaska Press, 2011, pp. 681–700.

[18] H. Eicken, B. Forbes, and H. Wiggins, "State of the Arctic conference 2010: International perspectives on progress of research responsive to decision-makers' information needs," *Ambio*, vol. 40, pp. 824–827, 2011.

[19] M. Tremblay *et al.*, "Communities and ice: Bringing together traditional and scientific knowledge," in *Climate Change: Linking Traditional Scientific Knowledge*. Winnipeg, MB, Canada: Univ. Manitoba, 2006, p. 289.

[20] C. Aporta, "The trail as home: Inuit and their pan-Arctic network of routes," *Hum. Ecol.*, vol. 37, pp. 131–146, 2009.

[21] S. Gearheard, G. Aipellee, and K. O'Keefe, "The Igliniit project: Combining Inuit knowledge and geomatics engineering to develop a new observation tool for hunters," in *SIKU: Knowing Our Ice*. New York, NY, USA: Springer, 2010, pp. 181–202.

[22] G. J. Laidler, P. Elee, T. Ikummaq, E. Joamie, and C. Aporta, "Mapping Inuit sea ice knowledge, use, and change in Nunavut, Canada (Cape Dorset, Igloolik, Pangnirtung)," in *SIKU: Knowing Our Ice: Documenting Inuit Sea Ice knowledge and Use*, I. Krupnik, C. Aporta, S. Gearheard, G. Laidler, and L. K. Holm, Eds. New York, NY, USA: Springer, 2010, pp. 45–80.

[23] C. Aporta, "Shifting perspectives on shifting ice: Documenting and representing Inuit use of the sea ice," *Can. Geographer/Le Géographe Canadien*, vol. 55, pp. 6–19, 2011.

[24] A. Fienup-Riordan and A. Rearden, "The ice is always changing: Yup'ik understandings of sea ice, past and present," in *SIKU: Knowing Our Ice: Documenting Inuit Sea Ice knowledge and Use*, I. Krupnik, C. Aporta, S. Gearheard, G. Laidler, and L. K. Holm, Eds. New York, NY, USA: Springer, 2010, pp. 295–320.

[25] J. D. Ford, T. Pearce, J. Gilligan, B. Smit, and J. Oakes, "Climate change and hazards associated with ice use in northern Canada," *Arctic, Antarctic, Alpine Res.*, vol. 40, pp. 647–659, 2008.

[26] C. Aporta and E. Higgs, "Satellite culture - Global positioning systems, Inuit Wayfinding, and the need for a new account of technology," *Curr. Anthropol.*, vol. 46, pp. 729–753, Dec. 2005.

[27] H. P. Huntington and S. Fox, "The changing Arctic: Indigenous perspectives," in *Arctic Climate Impact Assessment*, C. Symon, L. Arris, and B. Heal, Eds. New York, NY, USA: Cambridge Univ. Press, 2005, pp. 61–98.

[28] T. Bell, R. Briggs, R. Bachmayer, and S. Li, "Augmenting Inuit knowledge for safe sea-ice travel—The SmartICE information system," in *Proc. 2014 Oceans-St. John's*, 2014, pp. 1–9.

[29] J. P. Wilkinson *et al.*, "Tradition and technology: Sea ice science on Inuit sleds," *EOS, Trans. Amer. Geophys. Union*, vol. 92, pp. 1–4, 2011.

[30] P. Spencer, B. Graham, A. Barker, G. Timco, and B. Wright, "Construction aspects of building an evacuation route through rubble surrounding Beaufort Sea structures," in *Proc. Int. Conf. Port and Ocean Eng. Under Arctic Cond.*, POAC-07, Dalian, China, 2007.

[31] H. Eicken *et al.*, "Environmental security in Arctic ice-covered seas: from strategy to tactics of hazard identification and emergency response," *Marine Technol. Soc. J.*, vol. 45, pp. 37–48, 2011.

[32] A. Barker, G. Timco, and B. Wright, "Traversing grounded rubble fields by foot—Implications for evacuation," *Cold Regions Sci. Technol.*, vol. 46, pp. 79–99, 2006.

[33] P. Spencer, B. Graham, A. Barker, G. Timco, and B. Wright, "Construction aspects of building an evacuation route through rubble surrounding Beaufort sea structures," in *Recent Development of Offshore Engineering in Cold Regions*, vol. 2, Yue, Ed., Dalian, China: Dalian Univ. Technol. Press, 2007, pp. 823–832.

[34] M. L. Druckenmiller, H. Eicken, J. C. George, and L. Brower, "Assessing the shorefast ice: Iñupiat whaling trails off Barrow, Alaska," in *SIKU: Knowing Our Ice*. Dordrecht, The Netherlands: Springer, 2010, pp. 203–228.

[35] J. M. Jones *et al.*, "Landfast sea ice breakouts: Stabilizing ice features, oceanic and atmospheric forcing at Barrow, Alaska," *Continental Shelf Res.*, vol. 126, pp. 50–63, 2016.

[36] A. Mahoney, H. Eicken, and L. Shapiro, "How fast is landfast sea ice? A study of the attachment and detachment of nearshore ice at Barrow, Alaska," *Cold Regions Sci. Technol.*, vol. 47, pp. 233–255, Mar. 2007.

[37] M. A. Hopkins, J. Tuhkuri, and M. Lensu, "Rafting and ridging of thin ice sheets," *J. Geophys. Res., Oceans*, vol. 104, pp. 13605–13613, 1999.

[38] K. I. Ohshima, "Effect of landfast sea ice on coastal currents driven by the wind," *J. Geophys. Res., Oceans*, vol. 105, pp. 17133–17141, 2000.

[39] H. Eicken, T. Grenfell, D. Perovich, J. Richter-Menge, and K. Frey, "Hydraulic controls of summer Arctic pack ice albedo," *J. Geophys. Res., Oceans*, vol. 109, 2004, Art. no. C08007.

[40] D. A. Rothrock, D. B. Percival, and M. Wensnahan, "The decline in arctic sea-ice thickness: Separating the spatial, annual, and interannual variability in a quarter century of submarine data," *J. Geophys. Res., Oceans*, vol. 113, May 2008, Art. no. C05003.

[41] G. Spreen, R. Kwok, and D. Menemenlis, "Trends in Arctic sea ice drift and role of wind forcing: 1992–2009," *Geophys. Res. Lett.*, vol. 38, 2011, Art. no. L10709.

[42] R. Kwok, G. Spreen, and S. Pang, "Arctic sea ice circulation and drift speed: Decadal trends and ocean currents," *J. Geophy. Res., Oceans*, vol. 118, pp. 2408–2425, 2013.

[43] P. Rampal, J. Weiss, and D. Marsan, "Positive trend in the mean speed and deformation rate of Arctic sea ice, 1979–2007," *J. Geophys. Res., Oceans*, vol. 114, 2009, Art. no. C05013.

[44] X. Zhang, J. E. Walsh, J. Zhang, U. S. Bhatt, and M. Ikeda, "Climatology and interannual variability of Arctic cyclone activity: 1948-2002," *J. Clim.*, vol. 17, pp. 2300–2317, 2004.

[45] S. R. Stephenson, L. C. Smith, and J. A. Agnew, "Divergent long-term trajectories of human access to the Arctic," *Nature Clim. Change*, vol. 1, pp. 156–160, Jun. 2011.

[46] G. J. Laidler, T. Hirose, M. Kapfer, T. Ikummaq, E. Joamie, and P. Elee, "Evaluating the Floe Edge service: How well can SAR imagery address Inuit community concerns around sea ice change and travel safety?" *Can. Geographer/Le Géographe Canadien*, vol. 55, pp. 91–107, 2011.

[47] X. Wang, X. Cheng, F. Hui, C. Cheng, H. Fok, and Y. Liu, "Xuelong navigation in fast ice near the Zhongshan station, Antarctica," *Marine Technol. Soc. J.*, vol. 48, pp. 84–91, 2014.

[48] W. Abdalati *et al.*, "The ICESat-2 laser altimetry mission," *Proc. IEEE*, vol. 98, no. 5, pp. 735–751, May 2010.

[49] D. E. Shean *et al.*, "An automated, open-source pipeline for mass production of digital elevation models (DEMs) from very-high-resolution commercial stereo satellite imagery," *ISPRS J. Photogram. Remote Sens.*, vol. 116, pp. 101–117, 2016.

[50] B. Scheuchl, R. Caves, I. Cumming, and G. Staples, "Automated sea ice classification using spaceborne polarimetric SAR data," in *Proc. IEEE 2001 Int. Geosci. Remote Sens. Symp.*, 2001, pp. 3117–3119.

[51] M. Moen *et al.*, "Comparison of automatic segmentation of full polarimetric SAR sea ice images with manually drawn ice charts," *Cryosphere Discuss.*, vol. 7, pp. 2595–2634, 2013.

[52] M. Westoby, J. Brasington, N. Glasser, M. Hambrey, and J. Reynolds, "'Structure-from-motion' photogrammetry: A low-cost, effective tool for geoscience applications," *Geomorphology*, vol. 179, pp. 300–314, 2012.

[53] J. J. Koenderink and A. J. Van Doorn, "Affine structure from motion," *J. Opt. Soc. Amer. A*, vol. 8, pp. 377–385, 1991.

[54] M. A. Fonstad, J. T. Dietrich, B. C. Courville, J. L. Jensen, and P. E. Carbonneau, "Topographic structure from motion: A new development in photogrammetric measurement," *Earth Surf. Processes Landforms*, vol. 38, pp. 421–430, 2013.

[55] M. Nolan, C. Larsen, and M. Sturm, "Mapping snow-depth from manned-aircraft on landscape scales at centimeter resolution using structure-from-motion photogrammetry," *Cryosphere Discuss.*, vol. 9, pp. 333–381, 2015.

[56] D. O. Dammann, H. Eicken, A. Mahoney, F. Meyer, and S. Betcher, "Sea ice trafficability - New strategies for a changing icescape," submitted for publication.

[57] H. Eicken *et al.*, "A framework and database for community sea ice observations in a changing Arctic: An Alaskan prototype for multiple users," *Polar Geography*, vol. 37, pp. 5–27, 2014.

[58] J. C. George, H. P. Huntington, K. Brewster, H. Eicken, D. W. Norton, and R. Glenn, "Observations on shorefast ice dynamics in Arctic Alaska and the responses of the Iñupiat hunting community," *Arctic*, vol. 57, pp. 363–374, 2004.

[59] K. Brewster, "Northern Alaska Sea Ice Project Jukebox," 2016. [Online]. Available: http://jukebox.uaf.edu/seaice

[60] M. L. Druckenmiller, "Alaska shorefast ice: Interfacing geophysics with local sea ice knowledge and use," Doctoral dissertation, Univ. Alaska Fairbanks, Fairbanks, AK, USA, 2011.

[61] WMO, "World Meteorological Organization sea ice nomenclature," 2014. [Online]. Available: http://www.jcomm.info/index.php?option = com_oe&task = viewDocumentRecord&docID = 14598

[62] S. Filhol and M. Sturm, "Snow bedforms: A review, new data, and a formation model," *J. Geophys. Res., Earth Surf.*, vol. 120, pp. 1645–1669, 2015.

[63] M. B. Rivas, J. A. Maslanik, J. G. Sonntag, and P. Axelrad, "Sea ice roughness from airborne LIDAR profiles," *IEEE Trans. Geosci. Remote Sens.*, vol. 44, no. 11, pp. 3032–3037, Nov. 2006.

[64] A. Manninen, "Surface roughness of Baltic sea ice," *J. Geophys. Res., Oceans*, vol. 102, pp. 1119–1139, 1997.

[65] C. Liu, J. Chao, W. Gu, L. Li, and Y. Xu, "On the surface roughness characteristics of the land fast sea-ice in the Bohai sea," *Acta Oceanol. Sin.*, vol. 33, pp. 97–106, 2014.

[66] P. A. Moran, "Notes on continuous stochastic phenomena," *Biometrika*, vol. 37, pp. 17–23, 1950.

[67] Y. Chen, "New approaches for calculating Moran's index of spatial autocorrelation," *PLoS One*, vol. 8, 2013, Art. no. e68336.

[68] J. Lee and S. Li, "Extending Moran's index for measuring spatiotemporal clustering of geographic events," *Geographical Anal.*, vol. 49, pp. 36–57, 2016.

[69] J.-S. Lee and E. Pottier, *Polarimetric Radar Imaging: From Basics to Applications*. Boca Raton, FL, USA: CRC Press, 2009.

[70] F. T. Ulaby and C. Elachi, *Radar Polarimetry for Geoscience Applications*, vol. 1. Norwood, MA, USA: Artech House, 1990, 376 p. (No individual items are abstracted in this volume).

[71] W. Dierking, H. Skriver, and P. Gudmandsen, "SAR polarimetry for sea ice classification," in *Proc. Workshop POLinSAR, Appl. SAR Polarimetry Polarimetric Interferometry*, 2003, Paper 18.1.

[72] T. Eltoft, J. Grahn, A. Doulgeris, C. Brekke, L. Ferro-Famil, and B. Holt, "Multi-frequency polarimetric analysis of sea ice," in *Proc. 2013 Asia-Pac. Conf. Synthetic Aperture Radar*, 2013, pp. 96–99.

[73] J.-W. Kim, D.-J. Kim, and B. J. Hwang, "Characterization of Arctic sea ice thickness using high-resolution spaceborne polarimetric SAR data," *IEEE Trans. Geosci. Remote Sens.*, vol. 50, no. 1, pp. 13–22, Jan. 2012.

[74] K. Nakamura, H. Wakabayashi, K. Naoki, F. Nishio, T. Moriyama, and S. Uratsuka, "Observation of sea-ice thickness in the sea of Okhotsk by using dual-frequency and fully polarimetric airborne SAR (Pi-SAR) data," *IEEE Trans. Geosci. Remote Sens.*, vol. 43, no. 11, pp. 2460–2469, Nov. 2005.

[75] H. Wakabayashi, T. Matsuoka, K. Nakamura, and F. Nishio, "Polarimetric characteristics of sea ice in the sea of Okhotsk observed by airborne L-band SAR," *IEEE Trans. Geosci. Remote Sens.*, vol. 42, no. 11, pp. 2412–2425, Nov. 2004.

[76] E. Pottier and J.-S. Lee, "Application of the «H/A/alpha» polarimetric decomposition theorem for unsupervised classification of fully polarimetric SAR data based on the Wishart distribution," in *Proc. SAR Workshop, CEOS Committee Earth Observ. Satell.*, 2000, pp. 335–340.

[77] J.-S. Lee, M. R. Grunes, and R. Kwok, "Classification of multi-look polarimetric SAR imagery based on complex Wishart distribution," *Int. J. Remote Sens.*, vol. 15, pp. 2299–2311, 1994.

[78] B. Scheuchl, I. Cumming, and I. Hajnsek, "Classification of fully polarimetric single-and dual-frequency SAR data of sea ice using the Wishart statistics," *Can. J. Remote Sens.*, vol. 31, pp. 61–72, 2005.

[79] S. R. Cloude and E. Pottier, "A review of target decomposition theorems in radar polarimetry," *IEEE Trans. Geosci. Remote Sens.*, vol. 34, no. 2, pp. 498–518, Mar. 1996.

[80] A. Freeman and S. L. Durden, "A three-component scattering model for polarimetric SAR data," *IEEE Trans. Geosci. Remote Sens.*, vol. 36, no. 3, pp. 963–973, May 1998.

[81] J.-S. Lee, M. R. Grunes, T. L. Ainsworth, L.-J. Du, D. L. Schuler, and S. R. Cloude, "Unsupervised classification using polarimetric decomposition and the complex Wishart classifier," *IEEE Trans. Geosci. Remote Sens.*, vol. 37, no. 5, pp. 2249–2258, Sep. 1999.

[82] J.-S. Lee, M. Grunes, T. Ainsworth, L. Du, D. Schuler, and S. Cloude, "Unsupervised classification using polarimetric decomposition and complex Wishart classifier," in *Proc. 1998 IEEE Int. Geosci. Remote Sens. Symp.*, 1998, pp. 2178–2180.

[83] B. Scheuchl, R. Caves, I. Cumming, and G. Staples, "H/A/α-based classification of sea ice using SAR polarimetry," in *Proc. 23rd Can. Symp. Remote Sens.*, 2001, pp. 21–24.

[84] A. Ferretti, A. Monti-Guarnieri, C. Prati, F. Rocca, and D. Massonet, *InSAR Principles—Guidelines for SAR Interferometry Processing and Interpretation*, vol. TM-19. Paris, France: ESA, 2007.

[85] R. Bamler and P. Hartl, "Synthetic aperture radar interferometry," *Inverse Probl.*, vol. 14, 1998, Art. no. R1.

[86] K. Morris, S. Li, and M. Jeffries, "Meso-and microscale sea-ice motion in the East Siberian sea as determined from ERS-I SAR data," *J. Glaciology*, vol. 45, pp. 370–383, 1999.

[87] P. B. G. Dammert, M. Lepparanta, and J. Askne, "SAR interferometry over Baltic sea ice," *Int. J. Remote Sens.*, vol. 19, pp. 3019–3037, Nov. 1998.

[88] S. Li, L. Shapiro, L. McNutt, and A. Feffers, "Application of satellite radar interferometry to the detection of sea ice deformation," *J. Remote Sens. Soc. Jpn.*, vol. 16, pp. 67–77, 1996.

[89] D. O. Dammann, H. Eicken, F. Meyer, and A. Mahoney, "Assessing small-scale deformation and stability of landfast sea ice on seasonal timescales through L-band SAR interferometry and inverse modeling," *Remote Sens. Environ.*, vol. 187, pp. 492–504, 2016.

[90] F. J. Meyer, A. R. Mahoney, H. Eicken, C. L. Denny, H. C. Druckenmiller, and S. Hendricks, "Mapping arctic landfast ice extent using L-band syn-

thetic aperture radar interferometry," *Remote Sens. Environ.*, vol. 115, pp. 3029–3043, Dec. 2011.
[91] R. Scheiber, F. De Zan, P. Prats, L. S. A. Araújo, M. Künemund, and L. Marotti, "Interferometric sea ice mapping with TanDEM-X: First experiments," in *Proc. 2011 IEEE Int. Geosci. Remote Sens. Symp.*, 2011, pp. 3594–3597.
[92] A. Mahoney, D. O. Dammann, M. A. Johnson, H. Eicken, and F. J. Meyer, "Measurement and imaging of infragravity waves in sea ice using InSAR," *Geophys. Res. Lett.*, vol. 43, pp. 6383–6392, 2016.
[93] U. Wegmüller, C. Werner, M. Santoro, T. Strozzi, and A. Wiesmann, "ERS–ENVISAT TanDEM data over sea and shelf ice," in *Proc. FRINGE2009 Workshop*, Frascati, Italy, Nov. 30–Dec. 4, 2009 (ESA SP-677, Mar. 2010)
[94] W. Dierking, O. Lang, and T. Busche, "Sea ice local surface topography from single-pass satellite InSAR measurements: A feasibility study," *Cryosphere Discuss.*, vol. 11, pp. 1967–1985, 2017.
[95] E. Brower, private communication, 2015.

Dyre Oliver Dammann received the B.S. degree in meteorology from the University of Oslo, Oslo, Norway, in 2008, and the M.S. degree in meteorology and the Ph.D. degree in geophysics from the University of Alaska Fairbanks, Fairbanks, AK, USA, in 2011 and 2017, respectively.

He is currently a Postdoctoral Researcher in the Department of Earth, Space, and Environment, Chalmers University of Technology, Gothenburg, Sweden. His research interests include coastal sea ice properties and processes centered around sea ice system services and emerging needs of Arctic stakeholders. His research is particularly focused on expanding monitoring tools using synthetic aperture radar in support ice travel and on-ice operations of landfast sea ice.

Hajo Eicken received the Ph.D. degree in natural sciences from the University of Bremen, Bremen, Germany, in 1990.

He is a Professor of geophysics and the Director of the International Arctic Research Center, University of Alaska Fairbanks (UAF), Fairbanks, AK, USA. Over the past two decades, he helped establish a Coastal Sea-Ice Observatory in northern Alaska that provides an interface between geophysical, indigenous, and local knowledge of ice conditions and coastal hazards. At the UAF, he works to enhance use of scientific data by a range of different stakeholders at the local and international level, building on work initiated during the International Polar Year. His research interests include the growth, evolution, and properties of sea ice, as well as studies of ice use and ice hazards.

Andrew R. Mahoney received the Ph.D. degree in geophysics in 2006 from the University of Alaska Fairbanks, Fairbanks, AK, USA.

He is currently a Research Assistant Professor Geophysics with the University of Alaska Fairbanks. As the Leader of the Geophysical Institute's sea ice research group, he is actively engaged at the forefront of scientific efforts to better understand sea ice in the polar regions. His research interests are broad and interdisciplinary and include the study of sea ice in the context of its role in the global climate system, as a habitat for marine mammals, as an engineering constraint for maritime activities and its impact on other human activities in the Arctic. Through this research, he has developed significant expertise in polar remote sensing, particularly in the use of radar to study sea ice motion and deformation. He also has extensive field experience on sea ice, and during the past 17+ years, he has traveled widely throughout the Arctic studying sea ice on foot, by dogsled, by air, and from icebreakers. He has also wintered-over in Antarctica to study sea ice growth processes unique to the southern hemisphere. He is also known for his work with Arctic communities and efforts to integrate indigenous knowledge into polar research.

Eyal Saiet is currently working toward the Master's degree in remote sensing at the University of Alaska Fairbanks, Fairbanks, AK, USA.

For the past four years, he has been working as a Remote Sensing Technician in the Alaska Center Unmanned Aircraft System Integration. Through this role, he has initiated and supported many airborne remote sensing campaigns, and technologic advancement, at the UAS program. He particularly focuses on visible and thermal airborne remote sensing from the assembly of hardware into a payload, data acquisition, and processing that follow. He is particularly invested in harnessing photogrammetric techniques in his work to study environmental changes. Some of his work includes experimenting with photogrammetric products of different mediums such as sea-ice, tidewater glaciers, forest and tundra, and adding some automation algorithms into the future

Franz J. Meyer (S'03–A'03–M'04) received the Diploma in geodetic engineering and the Doctor of Engineering degree from the Technische Universität München, Munich, Germany, in 2000 and 2004, respectively.

From August 2000 to September 2003, he was with the Chair for Photogrammetry and Remote Sensing of the Technische Universität München, where he mainly worked on synthetic aperture radar (SAR) interferometry (InSAR) and differential InSAR technology development. From October 2003 to February 2007, he was a Senior Remote Sensing Scientist in the Remote Sensing Technology Institute, German Aerospace Center, Oberpfaffenhofen. There, his scientific work was focused on InSAR techniques for current and future SAR satellites (e.g., TerraSAR-X and TerraSAR-L), the conception of algorithms for traffic monitoring using SAR satellites (e.g., TerraSAR-X), the correction and modeling of atmospheric effects in InSAR data, and persistent scatterer interferometry. From March 2007 to September 2008, he was in the Alaska Satellite Facility (ASF), University of Alaska Fairbanks, Fairbanks, AK, USA, as a Research Scientist. Since October 2008, he has been in the Geophysical Institute, University of Alaska Fairbanks, where he currently holds the position of an Associate Professor for radar remote sensing. His current work includes studies of ionospheric and tropospheric effects on SAR and InSAR, new methods of InSAR time series analysis, SAR and InSAR applications, SAR processing, SAR data quality analysis, and integrating SAR into disaster monitoring workflows. Since 2014, he has also been the Chief Scientist of ASF, where he is responsible for interactions with the growing SAR user community, the generation of new value-added products, prototyping of on-demand services, as well as teaching SAR-related topics to the SAR science and applications communities. He is the author of more than 120 scientific publications, including five being acknowledged as "Best Papers."

Dr. Meyer received the IEEE Geoscience and Remote Sensing Society Gold Early Career Award 2011 for demonstrating outstanding ability and promise for significant contributions in the future.

John Craig George has been living in Utqiagvik (Barrow), AK, USA, since 1977. He received the B.S. degree in wildlife biology from the Utah State University, Logan, UT, USA, in 1976, and the Ph.D. degree in bowhead whale energetics, age estimation, and morphology from the University of Alaska Fairbanks, Fairbanks, AK, USA, in 2009.

He has been working as a Wildlife Biologist with the North Slope Department of Wildlife Management, Barrow, AK, USA, since 1982. Beginning in 1982, he worked on and later coordinated the bowhead whale ice-based population abundance project ("whale census") on the sea ice near Point Barrow for nearly two decades. He also has conducted hundreds of postmortem exams on bowheads harvested by Alaskan Eskimos. He has published a number of papers on this work ranging from evidence of killer whale predation to structural anatomy to population biology. He has been attending IWC meetings since 1987 focusing mainly on aboriginal whaling management procedures, assessments, and population estimation. He has also participated in studies of Eskimo traditional knowledge on the North Slope.